

Distant formation and differentiation of outer main belt asteroids and carbonaceous chondrite parent bodies

H. Kurokawa¹, T. Shibuya², Y. Sekine¹, B. L. Ehlmann^{3,4}, F. Usui^{5,6}, S. Kikuchi², and M. Yoda^{7,1}

¹Earth-Life Science Institute, Tokyo Institute of Technology, 2-12-1 Ookayama, Meguro-ku, Tokyo 152-8550, Japan

²Super-cutting-edge Grand and Advanced Research (SUGAR) program, Institute for Extra-cutting-edge Science and Technology Avant-garde Research (X-star), Japan Agency for Marine-Earth Science and Technology (JAMSTEC), 2-15 Natsushima-cho, Yokosuka 237-0061, Japan

³Division of Geological and Planetary Sciences, California Institute of Technology, Pasadena, California 91104, USA

⁴Jet Propulsion Laboratory, California Institute of Technology, Pasadena, California 91125, USA

⁵Institute of Space and Astronautical Science, Japan Aerospace Exploration Agency, 3-1-1 Yoshinodai, Chuo-ku, Sagamihara, Kanagawa, Japan

⁶Center for Planetary Science, Graduate School of Science, Kobe University, 7-1-48

Minatojima-Minamimachi, Chuo-Ku, Kobe, Hyogo 650-0047, Japan

⁷Department of Earth and Planetary Science, The University of Tokyo, 7-3-1 Hongo, Bunkyo-ku, Tokyo 113-0033, Japan

Key Points:

- Water-rock reactions and their products in asteroids are simulated by hydrological, geochemical, and spectral models.
- C-type asteroids with ammoniated phyllosilicates possibly formed beyond the NH₃ and CO₂ snow lines and differentiated.
- Carbonaceous chondrites can originate from rock-dominated inner cores of the differentiated bodies.

arXiv:2112.10284v1 [astro-ph.EP] 19 Dec 2021

Corresponding author: H. Kurokawa, hiro.kurokawa@elsi.jp

Abstract

Volatile compositions of asteroids provide information on the Solar System history and the origins of Earth's volatiles. Visible to near-infrared observations at wavelengths of $< 2.5 \mu\text{m}$ have suggested a genetic link between outer main belt asteroids located at 2.5–4 au and carbonaceous chondrite meteorites (CCs) that show isotopic similarities to volatile elements on Earth. However, recent longer wavelength data for large outer main belt asteroids show $3.1 \mu\text{m}$ absorption features of ammoniated phyllosilicates that are absent in CCs and cannot easily form from materials stable at those present distances. Here, by combining data collected by the AKARI space telescope and hydrological, geochemical, and spectral models of water-rock reactions, we show that the surface materials of asteroids having $3.1 \mu\text{m}$ absorption features and CCs can originate from different regions of a single, water-rock-differentiated parent body. Ammoniated phyllosilicates form within the water-rich mantles of the differentiated bodies containing NH_3 and CO_2 under high water-rock ratios (> 4) and low temperatures ($< 70^\circ\text{C}$). CCs can originate from the rock-dominated cores, that are likely to be preferentially sampled as meteorites by disruption and transport processes. Our results suggest that multiple large main belt asteroids formed beyond the NH_3 and CO_2 snow lines (currently > 10 au) and could be transported to their current locations. Earth's high hydrogen to carbon ratio may be explained by accretion of these water-rich progenitors.

Plain Language Summary

Small bodies record the Solar System history and how planets formed. Outer main belt asteroids are thought to be composed of bodies similar to carbonaceous chondrites (CCs) – meteorites which possibly sourced Earth's highly volatile elements. However, recent spectral observations suggest the presence of ammonia-bearing clays on several large asteroids. Ammonia-bearing clays are absent in CCs, and cannot easily form from materials stable in the current asteroid belt. To understand the conditions necessary to form minerals in those asteroids and CCs, we performed hydrological and geochemical modeling of water-rock reactions in these bodies. Synthetic spectra were computed for the model mineral assemblages and compared with asteroid observations using a space telescope. We found that surface minerals of outer main belt asteroids, including ammonia-bearing clays, form from starting materials containing NH_3 and CO_2 under water rich and low temperature conditions, while CC minerals form under water-poor conditions. We propose that multiple large outer main belt asteroids formed at distant orbits and differentiated to form different minerals in water-rich mantles and rock-dominated cores. Asteroid observations are looking at the product of water-rich mantles, whereas CCs preferentially sample the rocky cores. This scenario may also explain the elemental composition of Earth's volatiles.

1 Introduction

Volatile compositions of asteroids record Solar System history and the origins of Earth’s volatiles. The link between C-complex bodies and carbonaceous chondrite meteorites (CCs) has been suggested for a long time due to similarities in their spectral properties including the spectral slope, low albedo, and sharp $3\ \mu\text{m}$ absorption feature which is characteristic for hydrous minerals, centered at $\sim 2.7\ \mu\text{m}$ (Trigo-Rodríguez et al., 2014; Rivkin, Campins, et al., 2015). CCs show isotopic similarities to highly volatile elements on Earth (Dasgupta & Grewal, 2019), indicating CCs (and thus C-complex asteroids) as the origins of Earth’s volatiles. The molybdenum isotope dichotomy between CCs and non-carbonaceous meteorites (NCs) suggests their formation from distinct reservoirs (Kruijer et al., 2017). Large-scale dynamical evolution has been proposed to have delivered C-type bodies from the outer Solar System, possibly near or beyond the orbits of giant planets (e.g., Walsh et al., 2011). Volatile transport in the Solar System could take place also in the form of icy pebbles (T. Sato et al., 2016; Nara et al., 2019) and fragments of hydrated bodies (Trigo-Rodríguez et al., 2019).

However, a few large asteroids in the outer main belt possess additional absorption features at $3.1\ \mu\text{m}$ (King et al., 1992; Rivkin et al., 2006; Milliken & Rivkin, 2009; Takir & Emery, 2012), which are not observed in CCs. Several phases have been proposed as the sources of these absorption features. The $3.1\ \mu\text{m}$ absorption of 1 Ceres was attributed to ammoniated phyllosilicates or brucite (King et al., 1992; Milliken & Rivkin, 2009) before the arrival of the Dawn spacecraft. In situ observations by Dawn later confirmed that ammoniated phyllosilicates are widespread on the surface of Ceres (De Sanctis et al., 2015) (Figure 1b). The $3.1\ \mu\text{m}$ absorption feature of 24 Themis was attributed to water ice (Campins et al., 2010; Rivkin & Emery, 2010). Though several bodies have been classified as Ceres- or Themis-type by using ground-based observations (Takir & Emery, 2012; Rivkin et al., 2019), the dominant cause for the $3.1\ \mu\text{m}$ absorption features of large outer main belt asteroids has not been fully understood. Moreover, a fundamental question of why ammoniated phyllosilicates are present at least in some asteroids and absent in the CC collection has not been elucidated. As secondary minerals are the products of water-rock reactions in asteroid precursors (icy planetesimals), when their internal temperatures (T) are high enough to melt water ice, the difference in mineral assemblages should reflect that of water-rock reaction conditions. Water-rock reactions are also responsible for lithification of bodies initially accreted as porous aggregates by forming secondary aqueous alteration minerals (e.g., A. E. Rubin et al., 2007), in concert with compaction due to impacts (e.g., Bischoff et al., 2006; Blum et al., 2006; Trigo-Rodríguez et al., 2006; A. E. Rubin, 2012; Beitz et al., 2016; Tanbakouei et al., 2020).

Recently, the AKARI infrared space telescope obtained $2.5\text{--}5.0\ \mu\text{m}$ reflectance spectra of large main belt asteroids (mostly $> 100\ \text{km}$), which were free from the telluric absorption in prior ground-based data (Usui et al., 2019). AKARI revealed that $3.1\ \mu\text{m}$ absorption features are more common than previously thought (Figure 1b and Supplementary Figure 1). Detailed analysis of the $3.1\ \mu\text{m}$ features observed in AKARI spectra to identify the possible phases has not been performed yet.

We aim to understand the source of $3.1\ \mu\text{m}$ absorption features in outer main belt asteroid spectra and the reason why the material is present only in the above-mentioned asteroids and absent in CCs. Spectral analysis of AKARI data is performed, which leads to a conclusion that $3.1\ \mu\text{m}$ absorption features are mostly consistent with ammoniated phyllosilicates (Section 2). We perform geochemical modeling of water-rock reactions to show ammoniated phyllosilicates and more CC-like mineralogy form under high and low water-rock ratios (W/R, here defined as an effective mass ratio that tracks the total mass of water to which a unit mass of rock is exposed in the course of aqueous alteration) conditions, respectively (Section 3). Spectral modeling of model mineral assemblages is also performed to compare the synthetic spectra to observations (Section 4). We then introduce hydrological modeling of water circulation in asteroids to demonstrate that differ-

ent W/R can be sustained within a single body, namely, in the water-rich mantle and the rock-dominated core of an icy planetesimal (Section 5). Finally, we discuss the formation and evolution scenario for C-complex asteroids and CC parent bodies and its implications in Section 6, and conclude in Section 7.

2 Spectral analysis of asteroid observations using AKARI

2.1 AKARI data

We compared the spectra of C-complex asteroids and our model, especially at 2.7 μm and 3.1 μm , to constrain conditions of water-rock reactions for forming their surface minerals. D- and T-type asteroids are also considered because a spectral link to ungrouped CC Tagish Lake has been proposed (Hiroi et al., 2001), though a recent study over a broad spectral range does not support the idea (Vernazza et al., 2013). AKARI infrared space telescope obtained the reflectance spectra of 66 large main belt asteroids, 25 of which are C-complex and D- and T-type asteroids (Usui et al., 2019). We excluded the samples with unreliable spectra at any of the absorption bands we are interested in, following the criteria set by Usui et al. (2019) (the uncertainty in the reflectance to be $< 10\%$), and used the remaining 19 C-complex, 1 D-type, and 1 T-type asteroids (Supplementary Figure 1). We used Bus-DeMeo taxonomy as summarized by Hasegawa et al. (2017).

When available, the spectra of asteroids acquired using AKARI were compared with the ground-based telescope (NASA Infrared Telescope Facility, here after IRTF) data (Rivkin et al., 2003; Rivkin, Thomas, et al., 2015; Rivkin et al., 2019; Takir & Emery, 2012), as well as Dawn data for Ceres (Ciarniello et al., 2017) (Supplementary Figure 2). Because of telluric absorption, IRTF data are not available for the 2.7 μm absorption. Carbonate features at 3.4 μm are potentially important to constrain the conditions of water-rock reactions. However, we found deviation in this wavelength range between AKARI and IRTF data, possibly due to the contamination of neighboring stars, insufficient background subtraction, or incomplete thermal flux removal (Usui et al., 2019; Rivkin et al., 2019). Therefore, spectral comparison to the model results focused on 2.7 and 3.1 μm absorption features. We discuss implications for future observations to test our modeling with carbonate features (Section 6.5).

In order to discuss the possible contribution of brucite to 3.1 μm absorption while observing its 2.4 μm absorption, we combined the reflectance spectra acquired using AKARI (Usui et al., 2019) and ground-based observations (Bus & Binzel, 2002; DeMeo et al., 2009; Takir & Emery, 2012) for $> 2.5 \mu\text{m}$ and $< 2.5 \mu\text{m}$, respectively. Data were compiled by Hasegawa et al. (2017).

2.2 Methods

AKARI, Dawn, and model (see Section 4.1) spectra at 2.6–3.6 μm were fitted with 16th-order polynomials, and IRTF spectra at 2.9–3.6 μm were fitted with 8th-order polynomials to smoothen the noise, following Rivkin et al. (2019). Then, we calculated the absorption band depths, which are defined as follows (Usui et al., 2019):

$$D = \frac{R_c - R_\lambda}{R_c}, \quad (1)$$

where R_c is the continuum reflectance obtained by the interpolation of two local maximums across the absorption feature, and R_λ is the reflectance at the peak of absorption. When multiple absorption bands overlapped, we drew a common continuum to measure their depths (Supplementary Figure 3).

For error evaluation, we generated 10^6 different pseudo-observation spectra for each asteroid spectrum (taken either by AKARI, IRTF, or Dawn) by adding Gaussian noise. Standard deviation of the Gaussian function was assigned by observational uncertain-

ties reported in previous studies (Usui et al., 2019; Takir & Emery, 2012; Rivkin et al., 2003; Rivkin, Thomas, et al., 2015; Rivkin et al., 2019). Spectral fitting and band analysis were performed for each pseudo-observation spectrum. We computed the median and $1-\sigma$ (more precisely, 68% confidence interval) values by combining the obtained 10^6 absorption-band properties (center, depth, and width). When several IRTF spectra were available for a single asteroid, we computed the median and $1-\sigma$ values for each of spectrum and then calculated the average.

2.3 Results

We first performed an analysis of the $3.1 \mu\text{m}$ band shapes in asteroid spectra acquired using AKARI (Usui et al., 2019), as performed to distinguish possible phases on Themis and Ceres in previous studies (Rivkin, Campins, et al., 2015; De Sanctis et al., 2016). We found clear detection ($1-\sigma$) for ten bodies plus possible detection (band depths are nonzero at their median values but $1-\sigma$ error bars range to zero) for three (Figures 2 and Supplementary Table 1). Our spectral analysis of band centers showed that water ice-coating, whose absorption is centered at $\sim 3.08 \mu\text{m}$, was not responsible for these $3.1 \mu\text{m}$ absorption features in most cases but rather that Ceres-like ammoniated phyllosilicates with band centers $< 3.08 \mu\text{m}$ (Ehlmann et al., 2018) were consistent with the observed band centers (Figures 1b and 2). The observed absorption widths were also consistent with ammoniated phyllosilicates ($0.2\text{--}0.3 \mu\text{m}$) rather than water ice ($> 0.4 \mu\text{m}$). Among the 13 bodies, only one (24 Themis) was more consistent with water ice, and two others (52 Europa and 128 Nemesis) could be explained by either ammoniated phyllosilicates or water ice, or both.

Furthermore, AKARI spectra showed clustering into two groups in the 2.7 and $3.1 \mu\text{m}$ absorption depth plot (Figure 3). Bodies with deep ($> 20\%$) $2.7 \mu\text{m}$ absorption did not show $3.1 \mu\text{m}$ absorption, but those with shallow ($< 20\%$) absorption did. This suggests that the abundances of two phases responsible for $2.7 \mu\text{m}$ and $3.1 \mu\text{m}$ features are controlled by a single parameter, otherwise we would not see the correlation. As we show in Section 3.2, serpentine and ammoniated saponite are the candidates, as their abundances are controlled by a single parameter: the reaction W/R. We further show that our geochemical and spectral models can reproduce the trend seen in observations (Section 4.2).

We note that Rivkin et al. (2019) also analyzed $3.1 \mu\text{m}$ band centers in asteroid spectra with ground-based observation data. Their conclusions are consistent with ours in that $3.1 \mu\text{m}$ absorption features are more common on large outer main belt asteroids than previously thought, but they did not find a hiatus in the distribution to distinguish Ceres-like (ammoniated phyllosilicates) and Themis-like (water ice) objects. We utilized space telescope data which are free from telluric absorption around $3 \mu\text{m}$, analyzed the band widths as well as the center positions for a larger number of asteroid samples, and concluded that the majority of them were Ceres-like.

Because AKARI spectra contain wavy patterns possibly due to the contamination of neighboring stars or insufficient background subtraction (Usui et al., 2019), we also utilized independent spectra acquired using IRTF (e.g., Takir & Emery, 2012; Rivkin et al., 2019) and Dawn data for Ceres (Ciarniello et al., 2017). Comparison of $3.1 \mu\text{m}$ absorption showed quantitative consistency (Supplementary Figure 4 and Supplementary Table 1). Most importantly, two clusters were found in both AKARI and IRTF spectra (Supplementary Figure 5 and Supplementary Table 1). IRTF spectra showed shallower absorption than AKARI spectra, which might be caused by wavy patterns in AKARI spectra (Usui et al., 2019) or the artificial cutoff at $2.9 \mu\text{m}$ in IRTF spectra. Ceres spectra acquired by Dawn showed somewhat deeper absorption than AKARI and IRTF. We do not discuss the cause of quantitative difference further, but the origin of the qualitative trend observed in both AKARI and IRTF data is discussed (Section 4.2).

Additionally, the lack of correlation between 3.1 μm absorption depth and semi-major axis in the AKARI data (Supplementary Figure 6) as well as the short lifetime of water ice on asteroid surfaces in the main belt (Schorghofer, 2008; Beck et al., 2011; Brown, 2016) does not support water ice as the dominant source of these common features. We note that Takir and Emery (2012) and Rivkin et al. (2019) reported the correlation between the heliocentric distance and 3 μm absorption using a smaller number of samples and data set acquired using IRTF.

We also ruled out brucite as a major cause of the 3.1 μm absorptions on the main belt asteroids observed using AKARI. AKARI spectra combined with ground-based observation data (Hasegawa et al., 2017) did not show the 2.45 μm absorption (Supplementary Figure 7), which suggested the absence of brucite. The AKARI data thus indicate more Ceres-like, ammonium phyllosilicate-bearing asteroids than previously identified (Takir & Emery, 2012; Rivkin et al., 2019), increasing the need to explain the origin of ammonium, as NH_3 ice is unstable at those distances in the present Solar System.

Paradoxically, despite the fact that Ceres is the largest asteroid and several other large asteroids exhibit similar spectral properties, ammoniated phyllosilicates have not been found in CCs, such that the 3.1 μm absorption is not seen (Figures 1c and 3). Though long-term collisional evolution likely affected their mineralogy through gardening and mixing (Bischoff et al., 2006; Trigo-Rodríguez, 2015; Beitz et al., 2016; Nittler et al., 2019; Tanbakouei et al., 2020) and, consequently, infrared reflectance spectra, the common ammoniated features on many large asteroids, that dominate the mass of the asteroid belt and are thought to be primitive remnants of planetesimal formation (Bottke et al., 2005, 2015), require an explanation for their differences with CCs from their original water-rock reaction conditions, such as starting material composition, W/R, and T of alteration.

3 Geochemical modeling

3.1 Methods

Water-rock reactions in the molten stages of icy planetesimals were modeled. In the thermodynamic calculations, a mean composition of CV chondrites was assumed for the initial bulk rock (Pearson et al., 2006; Henderson et al., 2009; Clay et al., 2017) (Supplementary Table 2). Minor amounts of carbon, nitrogen, and chlorine were also included. In contrast to previous studies (M. E. Zolensky et al., 1989; Rosenberg et al., 2001; Schulte & Shock, 2004; McAlister & Kettler, 2008; Zolotov, 2012; J. Castillo-Rogez et al., 2018), our model explicitly computed the abundance of NH_4 -bearing phyllosilicates and solid solution, the former of which is the key mineral responsible for 3.1 μm absorption (e.g., Mg-saponite, Ehlmann et al., 2018), and we analyzed its stability for a wide range of temperatures and W/R.

W/R, a driving parameter in our simulation was explored for the range of $0.2 < \text{W/R} < 10$ (the mass ratio). For the initial fluid, three cases were assumed (Table 1). Whereas Case 1 simulated reactions of pure H_2O and the rock component as typically assumed for CC's parent bodies, Case 3 contained NH_3 and CO_2 in addition to H_2O , assuming accretion beyond the NH_3 and CO_2 snow lines. CO_2 concentrations were 0, 1 and 10 mol% (Cases 1–3, respectively) relative to H_2O while the latter two cases also included NH_3 (0.5%) and H_2S (0.5%). NH_3 and CO_2 were included to form ammoniated phyllosilicates and carbonates. H_2S was also considered because its snow line is close to those of NH_3 and CO_2 (Okuzumi et al., 2016) and it sources sulfur to form sulfur-bearing minerals. The model composition of Case 3 was established by considering comets as a reference. There is no significant bulk compositional variation between comets from the Kuiper belt or from the Oort cloud, and the abundances of CO_2 , NH_3 , and H_2S relative to H_2O range 2–30%, 0.3–1%, and 0.3–1%, respectively (the number of samples is about 10, Mumma

& Charnley, 2011; Bockelée-Morvan & Biver, 2017; M. Rubin et al., 2020). We assumed roughly averaged values in Case 3. Case 2 was the intermediate between the two with the reduced CO₂ abundances of at 1% relative to H₂O.

The equilibrium temperature and pressure were assumed to be 0, 100, 200, 300 and 350°C, and saturated vapor pressure of water. The temperatures used by our chemical equilibrium model correspond to the quenching temperature, i.e., the temperature at which water is no longer available for the reaction. After that time, the reactions are halted or slowed enough to preserve the minerals. Here we do not specify the mechanisms of quenching, which include freezing due to secular cooling (quenching at the freezing point), freezing due to abrupt temperature decrease, and abrupt water loss (quenching at the temperature). The latter two might be caused by events such as water exhalation (Young, 2001; Young et al., 2003) and catastrophic disruption (e.g., Jutzi et al., 2010). We note that complete consumption of water by reactions does not occur at $W/R > 0.2$. Considering serpentinization, the dominant water-rock reaction for low W/R , the critical value below which water consumption is complete is $W/R = 0.17$.

In the calculations, pyrene was considered as a representative of polycyclic aromatic hydrocarbon typically found in insoluble organic matter (IOM) while C1 compounds, except for CH₄, were included as soluble species (Zolotov, 2012). Because formation of some minerals (e.g., chlorite, olivine, clinopyroxene, garnet, mica, tephroite) is kinetically very slow at low temperatures, the precipitation of these minerals was suppressed in the thermodynamic calculations at temperatures lower than 100°C.

In the water-chondrite reactions, molecular hydrogen is generated due to reduction of water by metal iron and FeO in chondrites, which potentially elevates f_{H_2} of the fluid above H₂ saturation level in some cases. Therefore, it was assumed that f_{H_2} of fluid did not exceed water pressure (P_{H_2O}). When $f_{H_2} > f_{H_2O}$, the H₂ gas phase formed and was assumed to escape from the system.

The thermodynamic calculations of water-chondrite reactions were conducted using the EQ3/6 computer code (Wolery & Jarek, 2003). The thermodynamic database required for the calculations was generated using SUPCRT92 (Johnson et al., 1992) with thermodynamic data for minerals, aqueous species and complexes (Helgeson et al., 1978; Shock & Helgeson, 1988; Shock & Koretsky, 1995; Shock et al., 1989, 1997; Sverjensky et al., 1997; McCollom & Bach, 2009). Thermodynamic parameters for a series of smectites were estimated using the procedure published by Wilson et al. (2006).

3.2 Results

We quantified the mineral assemblages at chemical equilibrium for various W/R (0.2–10), T (0–350 °C), and NH₃ and CO₂ abundances, in which NH₄-bearing phyllosilicates were explicitly modeled. The key results are summarized in Figure 4 and all results are shown in Supplementary Figure 8.

Hydrous minerals represent the dominant phase at $T < 300^\circ\text{C}$, whereas anhydrous minerals become dominant at $T = 350^\circ\text{C}$ (Figure 4). The dominant hydrous phase was serpentine at lower W/R (e.g., $W/R < 4$ for Case 2), saponite at higher W/R (e.g., $W/R > 4$ for Case 2), and chlorite at higher T (e.g., $T = 350^\circ\text{C}$).

Ammoniated saponite appeared only when NH₃-ice was present in the starting material (Cases 2 and 3), at high W/R (> 4 and > 0.4 for Cases 2 and 3, respectively), and at $T \sim 0^\circ\text{C}$ (Figure 4). Lower W/R led to higher pH of rock-buffered fluids where the dominant hydrous phase was serpentine rather than saponite. Furthermore, at pH > 12 , NH₄-bearing saponite could not form due to the conversion of NH₄⁺ to NH₃ and H⁺ in the porewater. With the increasing temperature, NH₄-saponite was replaced with Fe-saponite at around 70°C (Figure 5). This happened because the low pH at high T

led to high concentrations of divalent ions, including ferrous ion, in fluids, which, in turn, stabilizes Fe(II) in the interlayer rather than NH₄-bearing saponite, consistent with a previous study (Neveu et al., 2017). The relative abundance of saponite and serpentinite as a function of W/R was consistent with previous studies (Neveu et al., 2017; J. Castillo-Rogez et al., 2018).

Carbonates appeared at high W/R and became more abundant as the CO₂ abundance increases from Cases 1 to 3. As W/R got lower, organics became stable instead of carbonates due to reduced conditions, caused by H₂ production and its high concentration.

4 Spectral modeling

4.1 Methods

The synthetic infrared reflectance spectra of model mineral assemblages remaining after the water-rock reactions were calculated by adopting the radiative transfer model for granular surfaces (Hapke, 2012) and compared with the AKARI data to constrain the conditions of water-rock reactions which formed minerals on large outer main belt asteroids and in CCs. Because the Hapke model does not fully reproduce the reflectance of dark mineral assemblages from mixing of endmembers (see, Kurokawa et al., 2020, and references therein), our purpose to use the spectral model was limited in demonstrating that our model could reproduce the observed trend in absorption depths, and we did not attempt to fully reproduce asteroid spectra (albedo, spectral slope, etc.) and constrain grain sizes. Because the reflectance spectra obtained using AKARI were given in the form of geometric albedo (also called physical albedo, which is the ratio of its actual brightness as observed from the light source to that of an Lambertian disk with the same cross-section), our model computed the geometric albedo A_p from the weighted average of the single scattering albedos (SSAs) of endmembers, $w(\lambda) = \sum f_i w_i(\lambda)$, where λ is the wavelength and f_i is the fractional relative cross section of component i . Assuming isotropic scatters, the geometric albedo $A_p(\lambda)$ is approximated by (Hapke, 2012),

$$A_p(\lambda) = 0.49r_0(\lambda) + 0.196r_0(\lambda)^2, \quad (2)$$

with an accuracy better than 0.4%, where $r_0(\lambda) = (1 - \gamma(\lambda))/(1 + \gamma(\lambda))$ is the diffusive (bihemispherical) reflectance, and $\gamma(\lambda) = \sqrt{1 - w(\lambda)}$. The endmember SSAs w_i were calculated through the refractive indices n and $k(\lambda)$ from the endmember reflectance spectra (more precisely, the reflectance factor, Hapke, 2012) $r_i(\lambda)$ taken from RELAB and the literature (Supplementary Table 3). The real refractive index n was assumed to be independent from the wavelength for the range considered here and was taken from the literature. The imaginary refractive index $k(\lambda)$ was calculated from the reflectance data and the given n value via the inversion of the Hapke model, as summarized by Lapotre et al. (2017). We assumed that grains were spherical, and the grain diameter for isotropic scatters was d . This modeling approach has been used and validated with natural samples and lab mixtures in previous studies (Lucey, 1998; Lawrence & Lucey, 2007; Lapotre et al., 2017).

Reflectance data for the wavelength range 2.5–4.0 μm were sometimes not found for minor minerals (NH₄-beidellite, tremolite, tephroite, sylvite, and Mn(OH)₂). We assumed the same refractive constants with NH₄-saponite for NH₄-beidellite, and neglected the optical effects of the others. Because the abundances of those minerals in our model are low, the assumption would not influence the calculated spectra.

We assumed that the grain diameter d was the same for all minerals except for IOM for simplification. The nominal size was $d = 100 \mu\text{m}$ for minerals and $d = 0.5 \mu\text{m}$ for IOM unless otherwise stated. The small grain size of IOM was assumed to increase its total cross section, and thus, to make the modeled albedo as low as those for the observed

asteroids. It is a well known problem that radiative-transfer models underestimate the influence of dark phases (see, Kurokawa et al., 2020, and references therein). For this reason previous studies (Rivkin & Emery, 2010; De Sanctis et al., 2015) assumed a very high abundance of amorphous carbon or magnetite. Our approach is in line with those studies. IOM particle sizes in meteorites are as small as assumed here (typically $< 1 \mu\text{m}$, e.g., Alexander et al., 2017) as well as other dark phases in the matrix (e.g., Buseck & Hua, 1993) which cause the low reflectance of CCs (Garenne et al., 2016; Kurokawa et al., 2020). Because Hapke’s SSA model cannot be applied to grain sizes smaller than the considered wavelengths, we assumed the same SSA (calculated from the measured reflectance) for IOM regardless of the grain size in order to avoid any unphysical behavior.

Thin coating of minerals by water ice has been proposed for the origin of $3.1 \mu\text{m}$ absorption on 24 Themis (Rivkin & Emery, 2010). To discuss the presence of water ice on asteroids’ surfaces to cause $3.1 \mu\text{m}$ absorption, we computed linear mixing of the water-ice coating model (Rivkin & Emery, 2010, Supplementary Figure 9) and the AKARI spectrum of an asteroid (2 Pallas) without $3.1 \mu\text{m}$ absorption. The band center and width were computed with the band detection method described in Section 2.2.

4.2 Results

Typical model spectra are shown in Figure 1a and all results are shown in Supplementary Figure 10. As expected, the diagnostic secondary minerals were seen in modeled spectra: hydrous minerals at $2.7 \mu\text{m}$, ammoniated phases at $3.1 \mu\text{m}$, and carbonates at $3.4 \mu\text{m}$ and $4.0 \mu\text{m}$. All modeled reflectance spectra showed a $2.7 \mu\text{m}$ OH-absorption. The diagnostic $3.1 \mu\text{m}$ absorption feature of ammoniated saponite appeared only when NH_3 -ice was present in the starting material (Cases 2 and 3), at high W/R (> 4 and > 0.4 for Cases 2 and 3, respectively), and $T \sim 0^\circ\text{C}$. Carbonate absorptions at $3.4 \mu\text{m}$ and $4.0 \mu\text{m}$ were seen for all modeled spectra, and got deeper when starting materials contain more carbon as CO_2 ice (Cases 1–3).

Comparison of the absorption depths between the model and AKARI observations indicates that high W/R (> 4 in Case 2), low T ($< 70^\circ\text{C}$), and fluids containing NH_3 and moderate CO_2 are required to form the surface mineralogy of several large main belt asteroids showing $3.1 \mu\text{m}$ features (Figure 1b). Observed spectra of both AKARI and IRTF samples showed clustering of two groups in the 2.7 and $3.1 \mu\text{m}$ absorption depth plot (Figure 3, Section 2.3). The clustering can be explained via the change in the dominant hydrous phase from serpentine to ammonia-bearing saponite with increasing W/R at $T = 0^\circ\text{C}$ with a single bulk volatile composition (either Case 2 or 3). The observed but relatively shallow $3.4 \mu\text{m}$ absorption observed in Ceres global average spectrum acquired using Dawn was consistent with an initial bulk composition depleted in CO_2 , compared to comets (Case 2 vs. Case 3, Figures 1a and 1b). In contrast, the bodies not showing the $3.1 \mu\text{m}$ absorption and CCs (Figure 1c) were reproduced either at lower W/R or at higher T ($> 70^\circ\text{C}$, Section 3.2), which led to the absence of NH_4 -saponite even though the starting material contained NH_3 ice.

Supplementary Figure 11 shows the dependence of absorption band depths on the grain sizes. Decreasing grain size d led to brighter overall reflectance and shallower absorption depths. Varying grain size covers a part of variation in observed absorption depths. Varying grain size from $200 \mu\text{m}$ down to $50 \mu\text{m}$ still showed qualitative similarity to the observations. This is important to note, as we do not know the actual grain sizes of asteroid surfaces to which we compared our model spectra. Thanks to the Dawn mission, Ceres is the best investigated body among them. However, estimates for its surface grain size varies between studies from a few μm to $\sim 100 \mu\text{m}$ (Prettyman et al., 2017; Li et al., 2019; Raponi et al., 2019; Kurokawa et al., 2020). Particles suspended in the water-rich mantle would be μm size initially (Neveu & Desch, 2015; Bland & Travis, 2017; Travis

et al., 2018), but extensive aqueous alteration may cause grain growth (e.g., Jones & Brearley, 2006).

These results suggest that secondary minerals of asteroids showing 3.1 μm absorption and of CCs formed under different W/R conditions ($W/R > 4$ and < 4 , respectively, in Case 2). Below, we hypothesize that such distinct conditions might be present in the water-rich mantle and porous rocky core of a single, water-rock differentiated body, and constrain the conditions to maintain the difference in W/R by simulating water flow in an icy planetesimal. We note that our term “differentiation” should not be confused with rock-metal differentiation. We discuss water-rock differentiation owing to segregation of rock grains to form a rock-dominated core.

5 Hydrological modeling

5.1 Methods

In order to investigate whether two different W/R values (higher and lower than 4 in the water-rich mantle and the rock-dominated core in Case 2) are possible within the same body, we performed hydrological simulations for the interiors of icy planetesimals. In contrast to previous studies (Travis & Schubert, 2005; Palguta et al., 2010; Bland & Travis, 2017; Travis et al., 2018), which modeled the entire body to demonstrate that compositional variation within a single planetesimal is possible, we focused on the velocity of fluid flow in the outer part of the porous rocky core. In this part, the temperature decreases toward the surface, which in turn could have potentially caused fluid convection in the core (e.g., Young et al., 2003). We employed a fluid-flow simulator called General purpose Terrestrial fluid-FLOW Simulator (GETFLOWS, Tosaka et al., 2000). GETFLOWS is a finite difference fluid-flow simulator that can solve movement of both surface water and subsurface fluid flows simultaneously. GETFLOWS can treat multi-phase components (i.e., water, gas, and solidified rock). Subsurface fluid flow was calculated based on Darcy’s equation and mass, momentum, and energy conservations. Given the low gravity of planetesimals, we employed vertically-variable gravitational acceleration, $g(r)$, based on the following equation: $g(r) = g_0 \cdot r/R$, where g_0 is the gravity at the surface, r is the radial distance from the center, and R is the radius of the planetesimal.

For simplicity, the computational area was discretized in a two-dimensional, Cartesian grid-block system (total length of 240 km with 120 grids and total depth of ~ 50 km with 21 grids). The use of Cartesian grid and ignoring spherical geometry is justified because we focus on a small domain in a planetesimal, rather than simulating the entire body. The uppermost grids (height of 10 km) of the grid-block system were defined as a water-rich layer without solidified rocks. The underlying 20 grids (height of 2 km for one grid) were composed of a mixture of fluid and solidified rocks. No heat production was assumed throughout the simulations. No exchange of fluids and heat with the outside of the grid-block system was also assumed.

The surface topography was based on a digital terrain model for an equatorial region of Ceres (longitude 160–190°E, Roatsch et al., 2016). The results were not sensitive to the surface topography, and we adopted Ceres topography as an example, as Ceres is the best investigated body among large C-complex asteroids.

The major parameters of our simulations were initial core temperature and gravity (i.e., the size of the planetesimal). We set the initial temperature of the bottom grids, T_{rock} , as 100°C or 300°C. The temperature of the overlying water-rich layer was kept at 0°C throughout the simulations. A linear thermal gradient was assumed for the initial temperature profile in the subsurface. In our simulations, the rocky core was cooled due to interactions (conduction or convection) with the low-temperature water-rich layer throughout the simulations. In reality, temperatures in planetesimals are dependent on

the timing of accretion (the amount of radioactive elements such as ^{26}Al), heat transport, and of course the time since the accretion, and thus variable temperatures between different bodies are possible. The above mentioned temperatures in our hydrological model were chosen to cover the temperature range where hydrous minerals are found to be stable in our geochemical modeling (Section 3.2) and the range in which various classes of CCs have experienced (Krot, Petaev, Zolensky, et al., 1998; Krot, Petaev, Scott, et al., 1998; Krot et al., 2006; Brearley, 2006).

As for gravity, we considered planetesimals with radius R of 200 or 500 km with the bulk density of 2000 kg/m^3 . In our spectral samples, only Ceres size is comparable to the latter, and the others ($R < \sim 250 \text{ km}$) can be approximated by the former.

We used the hydrological properties (viscosity, density, thermal expansion rate, and capillary pressure) of pure water (Tosaka et al., 2000) for fluids both in the porous core and in the water-rich mantle (the uppermost grids). In reality, the fluid contains fine grains and solutes (e.g., Travis et al., 2018), but their effects are expected to be minor. Assuming $W/R > 4$ (the mass ratio) as suggested from our geochemical model to form ammoniated phyllosilicates for the fluid, the increase in viscosity due to entrained fine particles are less than a factor of ~ 2 (particle volume concentration < 0.1 in Figure 3 of Travis et al., 2018). The difference in viscosity between pure water and brine is less than 10% for the low solute concentrations considered in our geochemical model (e.g., Kargel et al., 1991; Ozdemir et al., 2007). The freezing-point depression due to the solutes may affect the flow near the freezing point (Travis et al., 2018), but we focused on high-temperature phases where convection was intense and thus its influence is not important for our purpose.

The permeability k_p was randomly varied in the subsurface so that the distribution of permeability follows a Gaussian distribution with the mean value and standard deviation of $10^{-12 \pm 1} \text{ m}^2$. The mean permeability was based on the data for fine sands and those proposed for icy planetesimals (Grimm & McSween Jr, 1989; Cohen & Coker, 2000; Coker & Cohen, 2001; Young et al., 1999; Young, 2001; Young et al., 2003; McSween Jr et al., 2002; Travis & Schubert, 2005). The permeability depends on the particle size and porosity (Travis et al., 2018) and is lower for CCs (Bland et al., 2009). The adapted value is likely an upper limit, and we expect that the porosity would decrease with time as secondary minerals fills in the pore (as we observe in CCs, A. E. Rubin et al., 2007). If we assume lower values, flow becomes more sluggish and thus the difference in W/R would be sustained for even higher core temperatures (Section 5.2). Thus, our assumption on the permeability is a conservative approach.

The heat capacity, thermal conductivity, and porosity were assumed to be uniform in the subsurface as 1000 J/kg/K , 3.0 W/m/K , and 0.35 , respectively. We calculated time evolution of fluid temperature and pressure and their movements upon cooling of the porous rocky core. The results were analyzed using a data visualization software of ParaView 5.6.1.

5.2 Results

Figure 6 demonstrates snapshots of vector, velocity, and temperature of fluids in the subsurface at different initial core temperatures ($T_{\text{rock}} = 100$ and 300°C) and different sizes of planetesimals ($R = 200$ and 500 km in radius). Our results suggest that, at the high core temperatures and high gravity, various W/R and temperatures can be achieved within a single icy planetesimal. Convection of fluids occurred when $T_{\text{rock}} = 300^\circ\text{C}$ and $R = 500 \text{ km}$ (Figure 6a). Figure 6a shows that upwelling of hydrothermal fluids ($\sim 200\text{--}250^\circ\text{C}$) occurred at a high velocity of $0.2\text{--}0.4 \text{ mm/day}$ ($70\text{--}150 \text{ km/Myr}$). Downwelling of cold water from the water-rich layer also happened at velocity of $0.05\text{--}0.1 \text{ mm/day}$ ($20\text{--}40 \text{ km/Myr}$). It would take the order of ~ 1 Myrs for fluids to circulate within a $\sim 100\text{-km}$ -sized planetesimal given the fluid velocity of 0.1 mm/day (~ 40

km/Myr). Such a fluid circulation between the rocky core and water-rich layer continued for a few Myrs upon cooling. Due to the fluid circulation, the W/R was the highest along the fluid flow paths of the circulation cells. For instance, effective W/R in the fluid flow path increased (e.g., $W/R \sim 1$) a few times the local mass ratios that determined by porosity. In contrast, W/R remained low (e.g., $W/R \sim 0.3\text{--}0.5$) near the center of the circulation cells because of the lack of fluid input from the water-rich layer.

In contrast, at the low core temperatures and/or low gravity, the W/R in the rocky core remained low (the value close to the local mass ratio, e.g., $W/R \sim 0.3\text{--}0.5$) and distinct from that of the overlying water-rich mantle (e.g., $W/R > 4$ to form ammoniated phyllosilicates in Case 2, Section 3.2). No convection occurred for $T_{\text{rock}} = 100^\circ\text{C}$ and/or $R = 200$ km (Figure 6b–d). Under these initial conditions, fluids in the subsurface flew only through limited regions where permeability was locally high, forming veins in the rocky core. We note that the locations of upwelling and downwelling varied as we changed the random distribution of the permeability, but the general trend still held. Upon cooling and volume reduction of water, inhalations (single pass flow) of fluids occurred along with the veins. However, typical velocity of fluids at veins was 0.01–0.03 mm/day (3–10 km/Myr); accordingly, the W/R at veins would remain low even if inhalation occurred. We note that the fluid velocity obtained in our simulations was consistent with previous studies (e.g., ~ 10 km/Myr as shown in Figure 2A of Bland & Travis, 2017).

The difference in the modes of fluid flow dynamics (i.e., convection vs. inhalation) can be explained based on the Rayleigh-Darcy number, Ra (e.g., Young et al., 2003). The Rayleigh-Darcy number is expressed as follows based on the definition of the Rayleigh number and the Darcy’s law;

$$Ra = \frac{\rho\beta\Delta T k_p L g}{\alpha\eta}, \quad (3)$$

where ρ is the fluid density, β is the thermal expansion coefficient of fluid, ΔT is the temperature, k_p is the permeability, L is the length, g is the gravity, α is the thermal diffusivity, and η is the dynamic viscosity of fluid. When Ra is $< \sim 10^3$, no convection occurs in the system. Using the physical properties of pure water and our calculation conditions, Ra is less than $\sim 10^3$ for the 200 km planetesimal and/or initial core temperature of 100°C . If a planetesimal is 200 km or smaller, and/or if its core temperature is 100°C or less, no convection of pore water occurs. In contrast, Ra becomes $> 10^3$ for the 500-km planetesimal and initial core temperature of 300°C .

To summarize, the difference in W/R between the water-rich mantle and the porous rocky core was best maintained when $T_{\text{rock}} = 100^\circ\text{C}$ and/or $R = 200$ km (typical for our spectral samples). W/R in the core varied when $T_{\text{rock}} = 300^\circ\text{C}$ and $R = 500$ km (Ceres’ size). Though we do not fully rule out the latter case, high W/R to form ammoniated phyllosilicates might be achieved even in the core in this case.

6 Discussion

6.1 Formation and evolution scenario for outer main-belt asteroids

Based on the results presented in Sections 2–5, we propose a new idea that both Ceres-type materials containing ammoniated phyllosilicates and CCs-type materials formed in water-rock differentiated bodies which formed as icy planetesimals beyond the NH_3 and CO_2 snow lines and thus accreted NH_3 and CO_2 ice in addition to water ice (Figure 7, Stage 1). Their different mineral assemblages result from water-rock differentiation and consequent vertical gradients of W/R, temperatures, and pH within the single body. Assuming NH_3 and CO_2 sublimation temperatures of 75 and 85 K (Okuzumi et al., 2016), respectively, and the equilibrium temperature profile in the current Solar System $T_{\text{eq}} = 280 (r/\text{au})^{-1/2}$ K (where r is the orbital radius), the NH_3 and CO_2 snow lines are located at 11 and 14 au, respectively.

Parent bodies depleted in CO₂ compared to comets can best explain the amount of carbonates inferred from 3.4 μm and 4.0 μm absorption features of Ceres (Section 4.2). CO₂ depletion is expected as a consequence of degassing to space upon heating and melting of icy planetesimals (Figure 7, Stage 2). In order to quantify CO₂ degassing, we performed additional, low-temperature thermodynamic calculations of the H₂O-NH₃-CO₂ mixture with the cometary composition. We found that 90 wt.% of CO₂ was released from the mixture as gas at 0 °C, whereas NH₃ was retained as NH₄-hydrate fluid (Supplementary Text S1 and Supplementary Figure 12). This preferential loss of CO₂ to space led to the CO₂-depleted bulk composition relative to cometary ice (Case 2 composition, Section 3.2).

Further heating induced water-rock differentiation within bodies (Figure 7, Stage 2). While large, millimeter-sized grains (chondrules) settled down to form a low-W/R interior (porous rocky core), smaller grains (matrix) remained suspended by convection in water, forming a high-W/R upper-layer (ice-covered, muddy subsurface ocean) (Neveu & Desch, 2015; Bland & Travis, 2017; Travis et al., 2018). The upper layer water would be eventually lost to space via sublimation, but the observed 3.1 μm absorption feature of ammoniated phyllosilicates (Section 2.3) and high W/R (> 4) and low temperature ($< 70^\circ\text{C}$) conditions required to form these ammoniated phases (Section 3.2) indicate sufficient retention of subsurface water during heating so that these volatiles participated in water-rock reactions. The estimated lifetime of water ice on small bodies at the orbit of the main asteroid belt ($\sim 10^3$ – 10^4 years, Machida & Abe, 2010) is much shorter than the period of heating by radioactive decay ($\sim 10^6$ years, J. C. Castillo-Rogez & McCord, 2010). However, the spectral detection of water ice on 24 Themis (Campins et al., 2010; Rivkin & Emery, 2010) and the low bulk density of Ceres suggest that lifetime can be much longer, due to an insulating regolith layer (Schorghofer, 2008). Freezing prior to significant water loss led to the occurrence of the particular minerals formed at $T < 70^\circ\text{C}$, (namely, NH₄-saponite) and at W/R > 4 (carbonates) in the icy mantle (Figure 7, Stage 3). Alternatively, the prolonged lifetime of an H₂O-ice mantle can be naturally explained if the asteroids are delivered to the current location well after the freezing. After freezing, sublimation and loss of ice to space leave these secondary minerals on asteroid surfaces as lag deposits, causing their spectra around 3.1 μm being chiefly dominated by ammoniated phyllosilicates (not by water ice, Section 2.3).

Some of the observed asteroids did not show 3.1 μm absorption and resembled CM/CI chondrites (Section 4.2). These objects might have experienced insufficient water-rock differentiation, which led to lower W/R even in their upper layers, inhibiting ammoniated phyllosilicate formation even though the starting material contained NH₃ (e.g., Case 2 with low W/R, Section 3.2). Additionally, water loss prior to freezing due to exhalation (Young, 2001; Young et al., 2003) or catastrophic disruption (e.g., Jutzi et al., 2010) would leave only secondary minerals that were stable at higher T and lower W/R. Therefore, it is possible that these bodies accreted NH₃ and CO₂ ice but experienced a different evolution pathway.

Moreover, non-disruptive impacts through the Solar System history influenced asteroid surface compositions by removing and excavating endogenous materials and replenishing impactor materials. Decomposition of hydrous minerals due to impacts is expected to be limited (Wakita & Genda, 2019). Cumulative impacts have affected Ceres surface composition, though endogenous NH₄-bearing phyllosilicates still remain (Stein et al., 2019; Marchi et al., 2019). Such collisions are also responsible for compaction of these bodies and formation of a crust beneath the regolith layer (e.g., Bischoff et al., 2006; Blum et al., 2006; Trigo-Rodríguez et al., 2006; A. E. Rubin, 2012; Beitz et al., 2016; Tanbakouei et al., 2020).

Asteroid families can potentially be used to discuss whether impacts significantly influenced the observed surface materials (Supplementary Table 5). Among ten bodies showing clear 3.1 μm absorption, seven do not have families, while three (10 Hygiea, 24

Themis, and 128 Nemesis) do. Our spectral analysis suggests ammoniated phyllosilicates for Hygiea, water ice for Themis, and either one or both for Nemesis. Thus, the presence of the ammoniated-phyllosilicate features is mostly consistent with the absence of families which suggests preservation of ammoniated phyllosilicates.

Hygiea has been thought to have experienced a disruptive impact (Vernazza et al., 2020), but it shows an absorption feature consistent with ammoniated phyllosilicates. A possible explanation is incomplete loss of mantle materials upon the impact. Themis likely possesses water ice (Campins et al., 2010; Rivkin & Emery, 2010), which suggests that the family-forming impact did not lead to complete loss of water ice (Rivkin et al., 2014). This would also be applicable to Hygiea. Unless the impact completely removed the water-rich mantle, reaccumulation of fragments (Vernazza et al., 2020) and reformation of insulating lag deposit following sublimation of exposed water ice (Schorghofer, 2008) would keep the mantle materials.

In contrast, if the bodies which do not show the 3.1 μm absorption have families, it may suggest that impacts are responsible for the lack of ammoniated phyllosilicates. An example is 2 Pallas (Supplementary Table 5). Pallas is a heavily-cratered, high density ($2.92 \times 10^3 \text{ kg/m}^3$) body (Vernazza et al., 2021), and thus, it might be possible that Pallas was once water-rock differentiated but lost its water-rich mantle due to the impacts. However, many other bodies without the 3.1 μm absorption do not have families, suggesting that insufficient water-rock differentiation or the lack or loss of abundant water is a more plausible explanation for the absence of ammoniated phyllosilicates.

Observational limitation may also cause non-detection. In addition to clear detection for ten bodies, two showed the median 3.1 μm depths greater than 3% (but with their 1- σ ranges cover 0%, Supplementary Table 1). We only included one D-type asteroid, 361 Bononia, in our samples (Figure 3), but its 3.1 μm feature also supports a similar outer Solar System origin as suggested from isotopic analysis of carbonates in Tagish Lake meteorites (Fujiya et al., 2019).

The proposed interior model for large C-complex asteroids can be compared to that of Ceres, whose interior structure has been modeled based on gravity and shape measurements (Park et al., 2016; Ermakov et al., 2017; Mao & McKinnon, 2018). The inner core of our model is a mineral assemblage with a CM/CI-like composition whose density is $\sim 2400\text{--}3000 \text{ kg/m}^3$ (CM/CI chondrite grain densities, Consolmagno et al., 2008). This is an upper limit obtained at $W/R = 0.2$, and the density can be lower if water ice remains (in the case of $W/R > 0.2$). The density of the outer mantle is $\simeq 1200 \text{ kg/m}^3$ if $W/R = 4$ is assumed (20 wt.% serpentine/saponite mixture and 80 wt.% water ice, whose densities are 2500 kg/m^3 and 900 kg/m^3 , respectively), and it can be lower if $W/R > 4$ (more ice remains). This is in good agreement with the two-layer model for Ceres: $\simeq 2400 \text{ kg/m}^3$ and $1200\text{--}1400 \text{ kg/m}^3$ for the inner and outer layers (Ermakov et al., 2017).

6.2 Formation and evolution scenario for CCs

If ammoniated phyllosilicates are more widespread on outer main belt asteroids than previously thought (Section 2.3), their absence in CCs requires an explanation. A parsimonious explanation is that CCs and C-complexes formed at similar locations beyond the NH_3 and CO_2 snow lines at different W/R . While asteroid observations inform the relics of near-surface water-rock reactions, we propose that meteorites chiefly sample the inner, low- W/R part (Figure 7, Stage 4). In addition to the fact that our spectral model for Case 2 with $W/R < 1$ reproduced CCs' spectral features (Section 4.2), the model mineral composition (Figure 4) showed general agreement with secondary minerals in CM/CI chondrites, namely, the abundant hydrous phyllosilicates (serpentine), organic compounds (represented by pyrene in our geochemical model), pyrrhotite (troilite), magnetite, and carbonates (e.g., A. E. Rubin, 1997a, 1997b). Preferential sampling of rock-dominated cores as CCs is possible because the inner core dominates the volume of an asteroid's

rocky material and is less fragile upon collisional disruption compared to the ice-dominated mantle and the upper-most regolith layer, due to lithification caused by secondary mineral formation in pore space (e.g., A. E. Rubin et al., 2007). Aqueous alteration takes place also in the water-dominated mantle. However, its high W/R (>4) causes water to be mostly left as ice, inter-mixed with rocky grains. Such ice is stable in the subsurface of large asteroids, but collisionally-produced ice-cemented fragments would be disaggregated as ice is not stable in the inner Solar System. Ice sublimation will cause efficient disruption of the fragments down to the rock grain scale, as we observe main belt comets which release dust likely due to ice sublimation (e.g., Hsieh & Jewitt, 2006; Hsieh et al., 2018).

According to our hydrological simulations, W/R of the rocky core would remain low (< 1) except for the uppermost grids of the core (the thickness = 2 km) due to inhibition of effective porewater convection if the interior temperature was $< 200^\circ\text{C}$ and/or the planetesimal radius was < 500 km (Section 5.2). The former and the latter are applicable for Ceres and the rest of our spectral samples, respectively. The conditions of low W/R resulted in the absence of NH_4 -bearing saponite and the limited amount of carbonates (Section 3.2). Exhaustion of water from the interior before freezing, if it happened, would result in the occurrence of secondary minerals (e.g., chlorite) that are stable at temperature higher than 0°C as suggested for some classes of CCs (M. Zolensky et al., 1993).

Petrographic evidence and aggregate accretion theory are in favor of CC parent bodies being water-rock differentiated (Bland & Travis, 2017). Furthermore, low W/R independently estimated from oxygen isotopes (Marrocchi et al., 2018) and bulk chemistry (Alexander, 2019) are particularly consistent with the inner-core origin, otherwise W/R would be comparable or higher than the nebular value (~ 1). The inner-core origin has been suggested for CI chondrites and Tagish Lake from the lack of their asteroid analogues (Vernazza et al., 2017), but here we extend the idea to all classes of hydrous CCs. Although we do not rule out formation inside the NH_3 and CO_2 snow lines for some of the CCs (Case 1, Section 3.2), bulk elemental and isotopic studies concluded that CC water could have a common origin (e.g., Alexander, 2019, and references therein), suggesting that all CCs possibly formed beyond the NH_3 and CO_2 snow lines.

Organic molecules have been suggested as a possible alternative source of NH_3 on Ceres (McSween Jr et al., 2018), but our estimation showed that efficient release of NH_3 from IOM was required to produce the amount of ammoniated phyllosilicates to cause the observed $3.1 \mu\text{m}$ absorption features. The highest nitrogen abundance in CC IOM is 2.7 wt.% (Pizzarello & Williams, 2012). Even if the original chondritic rock is assumed to contain 4 wt.% of IOM, which is the highest organic content in CCs (Alexander et al., 2012), the nitrogen content in CCs is calculated to be 0.108 wt.%. This value corresponds to approximately 3.7 wt.% ammoniated saponite in CCs even if the heaviest member of the smectite solid solution, iron-rich ammoniated saponite, is assumed. In comparison, our spectral calculations indicated that >10 wt.% of ammoniated saponite was required to explain the observed $3.1 \mu\text{m}$ absorption features (Figures 3 and 4), though an extensive parameter survey changing grain sizes of all phases showed that a lower abundance down to 1 wt.% was possible at least for Ceres (Kurokawa et al., 2020). Moreover, such efficient release of ammonia requires $\sim 300^\circ\text{C}$ (Pizzarello & Williams, 2012; McSween Jr et al., 2018), which is much higher than estimated temperatures experienced by CM/CIs (Krot et al., 2006). Therefore, we suggest that accretion of NH_3 ice provides a better scenario to account for both asteroid observations and analysis of CCs. We note that icy planetesimals might possess variable abundances of organic compounds. A higher abundance of organics has been proposed for bulk Ceres (Zolotov, 2020) as its surface likely contains a higher amount of organic compounds than CCs (Prettyman et al., 2017; Kurokawa et al., 2020).

Assuming that CCs are not fundamentally different from the large C-complex asteroids with 3.1 μm absorption features that occupy much of the mass of the outer main belt, this model explains why the mineralogy of CCs – the lack of NH_4 -saponite and the low abundance of carbonates – differs from the asteroid observations. Telescopic observations of C-complex asteroids and laboratory analysis of CCs are looking at the products in the water-rich, near-surface mantle or rocky core of the same system, respectively.

We note that our hypothesis indicating preferential sampling of rock-dominated cores of water-rock differentiated bodies as CCs does not necessarily mean that all CCs originated from the cores. None of Ch and Cgh asteroids in our samples showed 3.1 μm absorption (Supplementary Table 5). These types of asteroids have been proposed to be the origins of CM2 chondrites (Burbine, 1998).

6.3 Relevant timescales

Our scenario assumed that aqueous alteration proceeded after water-rock differentiation. The timescale of differentiation after ice melting is $\sim 10^{4-5}$ years (Bland & Travis, 2017). The temperature is buffered at 0°C for a longer period owing to the latent heat of ice melting ($\sim 10^{5-6}$ years, Bland & Travis, 2017). Experimental estimates of reaction times at low temperatures are extremely difficult (e.g., Jones & Brearley, 2006), but the alteration would be very slow. For example, Jones and Brearley (2006) measured phyllosilicate formation timescales to be days to weeks at 150–200°C via experiments using Allende CV3 carbonaceous chondrite, and estimated the alteration timescale to be $\sim 10^{4\pm 2}$ years at 25°C by extrapolation. It would be much slower at 0°C. Additionally, extrapolating dissolution rates down to 0°C led to the timescale estimation to be $\sim 10^5$ years and $\sim 10^6$ years for 100 μm grains of olivine and enstatite, respectively, at pH ~ 12 (estimated based on kinetic parameters given by Palandri & Kharaka, 2004). Thus, although some reactions might have proceeded during sedimentation of grains, the majority of aqueous alterations would have proceeded after water-rock differentiation.

Once internal heating overcomes the latent heat of ice melting, the temperature increases above 0°C. The water-rock reactions assumed in our model are faster than the fluid circulation (Myrs) in the hypothetical planetesimals (200 and 500 km in radius) at, for instance, 25°C (Jones & Brearley, 2006), suggesting that a near-equilibrium state between rock and fluid could be maintained each time and everywhere in planetesimals even if W/R and temperature slowly changed during global fluid circulation (of course, fluid vaporization during water-rock reactions and textural insulation by alteration minerals can generate large- and small-scale disequilibria, respectively, as inferred from meteorites). The sluggish flow may explain CC features which suggest the dominance of static aqueous alteration (Trigo-Rodríguez & Rubin, 2006; A. E. Rubin et al., 2007; Trigo-Rodríguez et al., 2019), while fluid flow in planetesimals (Young et al., 1999) was assumed in our model.

In the proposed scenario (Figure 7), accretion (Stage 1) should have been completed at < 4 Myrs from calcium–aluminium-rich inclusion formation to initiate water-rock differentiation (e.g., Bland & Travis, 2017). This timescale has also been constrained from the onset time of aqueous alteration informed from the Mn-Cr system in CC carbonates (Fujiya et al., 2013; Lee et al., 2012, 2013). The accretion timescale is consistent with dust coagulation models (e.g., Okuzumi et al., 2012) and with the existence of substructures in Myrs-old protoplanetary disks in a few tens of au scale (e.g., Andrews et al., 2018), which may be signatures of ongoing planetesimal formation. After accretion, differentiation and alteration started in ~ 1 Myr (e.g., Bland & Travis, 2017). Time of freezing (Stage 3) depends on the sizes of planetesimals (Wakita & Sekiya, 2011). Complete H_2O loss via sublimation to space depends on the size and heliospheric distance (Schorghofer, 2008) and likely takes longer than the age of the Solar System for large asteroids, as water ice likely exists in Ceres and on Themis (Campins et al., 2010; Rivkin & Emery, 2010).

We note that the proposed scenario for the distant origin is not sensitive to the timing of migration, as long as the majority of accretion takes place prior to migration.

6.4 Implications for planet formation

Our hypothesis that C-complex asteroids and CC parent bodies accreted NH_3 and CO_2 ice is new, but it is naturally expected from the modern planet formation theory. Radial mixing of small bodies due to gravitational scattering by gas giants in the Grand Tack scenario (e.g., Walsh et al., 2011) assumes that C-type asteroids originate from near or beyond giant planet formation regions, namely, beyond the NH_3 and CO_2 snow lines (currently > 10 au). Alternatively, NH_3 and CO_2 ice might be delivered directly to bodies formed in the main belt via icy pebbles, following the inward migration of these snow lines in the late stage of the solar nebula evolution (De Sanctis et al., 2015; Nara et al., 2019). Direct evidence of icy pebble accretion is difficult to find, but a carbon-rich clast in a CR chondrite (Nittler et al., 2019) might be an example of migration and accretion of such small fragments.

We proposed that C-complex and CCs parent bodies formed with a comet-like composition, but this does not necessarily mean that C-complex asteroid precursors are equivalent to comets. Rather, the difference in deuterium to hydrogen ratio between CCs and comets (Alexander et al., 2012) suggest that they formed from different reservoirs in the solar nebula. In addition to the NC/CC dichotomy (Kruijjer et al., 2017), there should have been at least another distinct reservoir to separate CC- and comet-building materials in the early Solar System. Our study suggests that at least the latter boundary was located beyond the NH_3 and CO_2 snow lines. Thus, mechanisms to partition reservoirs in the solar nebula were not limited to early formation of Jupiter (Kruijjer et al., 2017; Desch et al., 2018). A pressure maximum near Jupiter’s location in the solar nebula, which halts inward migration of pebbles, has been proposed as an alternative origin of NC/CC dichotomy (Brasser & Mojzsis, 2020). We suggest that there might be multiple pressure traps to separate reservoirs. Possible origins of pressure traps include gas-dust viscous gravitational instability (Tominaga et al., 2019), magneto-hydrodynamical wind (Taki et al., 2021), sublimation near the snow line(s) (Charnoz et al., 2021), and disk–planet interaction (Kanagawa et al., 2015). Such multiple pressure traps in a single protoplanetary disk are thought to create ringed structures which were found to be common in protoplanetary disks observed recently by the Atacama Large Millimeter/submillimeter Array (the spacial scales of rings are several tens of au, Andrews et al., 2018; Dullemond et al., 2018). A ringed structure supported by multiple pressure traps may be important for formation of planetesimals and planets in our Solar System, as well as extrasolar systems (Johansen et al., 2014; Morbidelli, 2020).

Bulk W/R of CC parent bodies was proposed to be higher than those recorded for CCs in our study, which may explain the disagreement in volatile compositions between bulk silicate Earth (BSE) and chondrites. BSE has higher hydrogen to carbon ratio (H/C) than the chondritic value (Hirschmann & Dasgupta, 2009; Dasgupta & Grewal, 2019), which was expected in our model. A fraction of small bodies transferred inward from the outer Solar System would have been captured in the main belt, while others accreted onto Earth during its formation, contributing substantial water and leading to Earth’s high H/C ratio.

6.5 Implications for sample return missions and future observations

The proposed new paradigm can be tested in the near future by return samples from small carbonaceous asteroids by Hayabusa2 (Watanabe et al., 2019) and OSIRIS-REx (Lauretta et al., 2017). Our model (Case 2, W/R < 1 , Section 3.2) predicts that returned samples may contain trace amounts of NH_4 -bearing salts (halite) and/or NH_3 - (and possibly CO_2 -) bearing fluid inclusions. These would be easily lost from CCs in terrestrial

environments due to deliquescence, as they are rarely found in meteorites except for few examples, such as halite in Zag and Monahans (1998) (M. E. Zolensky et al., 1999; Whitby et al., 2000; A. E. Rubin et al., 2002; Chan et al., 2018), but could be found in returned samples. Remote detection of carbonates (Kaplan et al., 2020) and possible existence of nanophase magnetites which causes its “blue” spectral slope due to space weathering on Bennu (Trang et al., 2021) are also consistent with model prediction (a few wt.% in Case 2 at $W/R < 1$ and $T = 0^\circ\text{C}$, Figure 4).

Large C-complex main-belt asteroids with ammoniated-phyllsilicate features were proposed to have the same origin with CCs’ parent bodies in our scenario. The sample return from these asteroids (e.g., from Ceres, Burbine & Greenwood, 2020; Gassot et al., 2021; J. Castillo-Rogez et al., in press) is ultimately needed to understand their building blocks and evolution history. The proposed scenario predicts that they would show the isotopic similarity to CCs, but not to comets. After the submission of this study, Tsuchiyama et al. (2021) reported CO_2 fluid trapped in a CC. They suggested that its parent body accreted CO_2 ice beyond the CO_2 snow line, which is fully consistent with our scenario for the CC origins.

Future asteroid observations are also useful to test the proposed model. Our geochemical model predicts that the abundance of carbonates correlates with that of ammoniated saponite (Section 3.2), which should be visible in their 3.4 and 4.0 μm absorptions (Section 4.2). Carbonates were found on Ceres (De Sanctis et al., 2015) as well as Bennu (Kaplan et al., 2020). AKARI and IRTF spectra at these wavelengths do not agree with each other, suggesting that they are severely influenced by, for example, the thermal component (Section 2.1). Observations of asteroids showing 3.1 μm absorption with improved accuracy at these longer wavelengths would be particularly useful to test our hypothesis. Moreover, increasing the number of samples, especially including smaller sizes are important. Although our samples are mostly larger than 100 km and do not show clear correlation between the size and ammoniated-phyllsilicate features (Supplementary Figure 6), we predict that much smaller bodies tend to lack these features.

7 Conclusions

We combined spectral analysis of large outer main belt asteroids observed using the AKARI space telescope ($> 2.5 \mu\text{m}$) and hydrological, geochemical, spectral modeling of water-rock interactions in icy planetesimals and their products to understand the origin of C-complex asteroids showing 3.1 μm absorption features and their relations to CCs. We have come to the following conclusions. i) Our spectral analysis showed that the positions and widths of the absorption band are more consistent with ammoniated phyllosilicates than water ice for the majority of samples. Brucite was also ruled out as the source of absorption features by combining ground-based data for shorter wavelengths ($< 2.5 \mu\text{m}$). ii) Our geochemical model combined with synthetic spectral calculations showed that the surface materials of outer main belt asteroids showing 3.1 μm absorption features of ammoniated phyllosilicates can form from starting materials containing NH_3 and CO_2 ice through water-rock reactions in water-rich ($W/R > 4$) and low temperature ($< 70^\circ\text{C}$) conditions. In contrast, CC-like mineral assemblages forms in relatively water-poor ($W/R < 4$) and/or high temperature ($> 70^\circ\text{C}$) conditions. iii) Our hydrological model demonstrated that such difference in W/R can be maintained in a single, water-rock differentiated body, if the interior temperature is $\lesssim 100^\circ\text{C}$ (for the largest asteroid Ceres) and/or the planetesimal radius is $< 500 \text{ km}$ (all of our spectral samples except for Ceres).

Based on these results, we proposed that several, if not all, C-complex asteroids and CC parent bodies formed beyond NH_3 and CO_2 snow lines and differentiated. Surface minerals containing ammoniated phyllosilicates and CC-like materials formed in the water-rich mantles and in the rock-dominated cores of the water-rock differentiated bod-

ies, respectively. The materials in the rocky cores are less fragile due to lithification and thus more likely to be sampled as meteorites. The distant origin of C-complex asteroids is naturally expected from the modern planet formation theory which involves Solar System-scale migration of pebbles and planetesimals. Moreover, the hypothesized water-rich progenitors of C-complex asteroids and CCs can, if they accreted onto early Earth, explain why the H/C ration of Earth is higher than that of CCs. Finally, our hypothesis can be tested via sample return missions by looking for NH_4 -bearing salts (halite) and/or NH_3 - (and possibly CO_2 -) bearing fluid inclusions, as well as future asteroid observations by testing the correlation of $3.1 \mu\text{m}$ ammoniated phase with $3.4 \mu\text{m}$ and $4.0 \mu\text{m}$ carbonate features.

Author contributions statement

H.K. and B.E. performed the spectral calculations. T.S. and S.K. performed the thermodynamic calculations for water-rock reactions. Y.S. performed water circulation simulations. F.U. compiled the asteroid observation data. M.Y. performed thermodynamic calculations for ice mixtures. All authors designed the project and wrote the manuscript.

Additional information

The authors declare no competing interests.

| Name | CO ₂ [mol%] | H ₂ S [mol%] | NH ₃ [mol%] | Note |
|--------|------------------------|-------------------------|------------------------|--|
| Case 1 | 0 | 0 | 0 | Pure water and rock |
| Case 2 | 1 | 0.5 | 0.5 | Cometary composition, CO ₂ depleted |
| Case 3 | 10 | 0.5 | 0.5 | Cometary composition |

Table 1. Volatile abundance relative to water in our geochemical model.

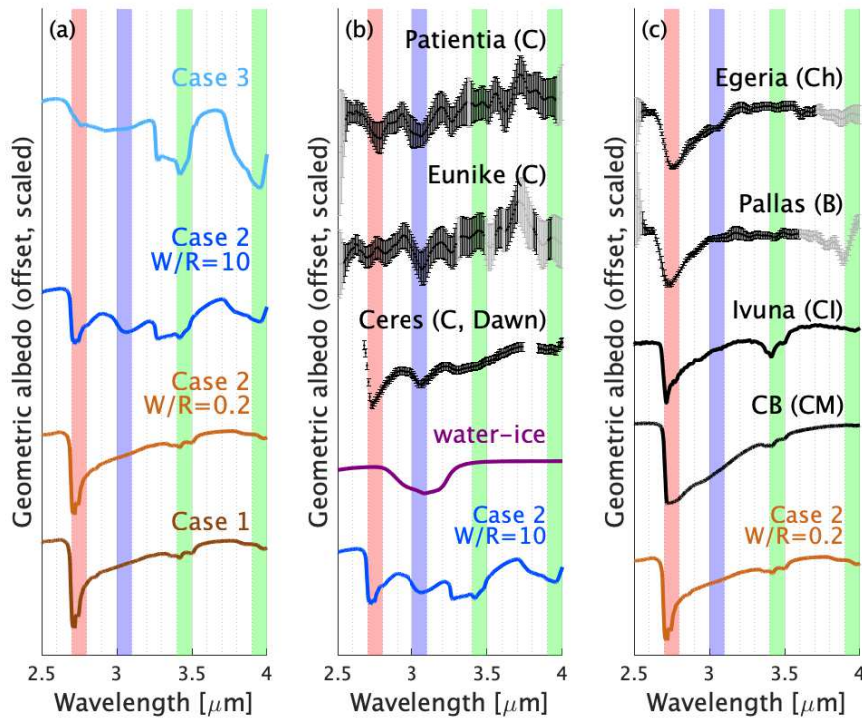


Figure 1. Comparison between models and observed infrared reflectance spectra. (a) Model spectra. Brown line: Case 1, $T = 0^\circ\text{C}$, and $W/R = 10$. Orange line: Case 2, $T = 0^\circ\text{C}$, and $W/R = 0.2$. Blue line: Case 2, $T = 0^\circ\text{C}$, and $W/R = 10$. Cyan line: Case 3, $T = 0^\circ\text{C}$, and $W/R = 10$. (b) Spectra of asteroids showing 2.7, 3.1, and 3.4 μm absorption features compared to the Case 2 model and the water-ice coating model (Rivkin & Emery, 2010). (c) Spectra of asteroids and CM/CI chondrites showing a dominant 2.7 μm absorption feature. Observed spectra were scaled and offset to compare the absorption features (see Supplementary Figures 1 and 10 for the original spectra). The gray data points indicate unreliable wavelength regions due to large uncertainties defined by Usui et al. (2019). We highlighted the position of three absorption features. Red area: 2.7 μm (hydrous minerals). Blue area: 3.1 μm (ammoniated phyllosilicates or water ice). Green area: 3.4 and 4.0 μm (carbonates). AKARI, Dawn, and meteorite data are from Usui et al. (2019), Ciarniello et al. (2017), and the references in Supplementary Table 4, respectively.

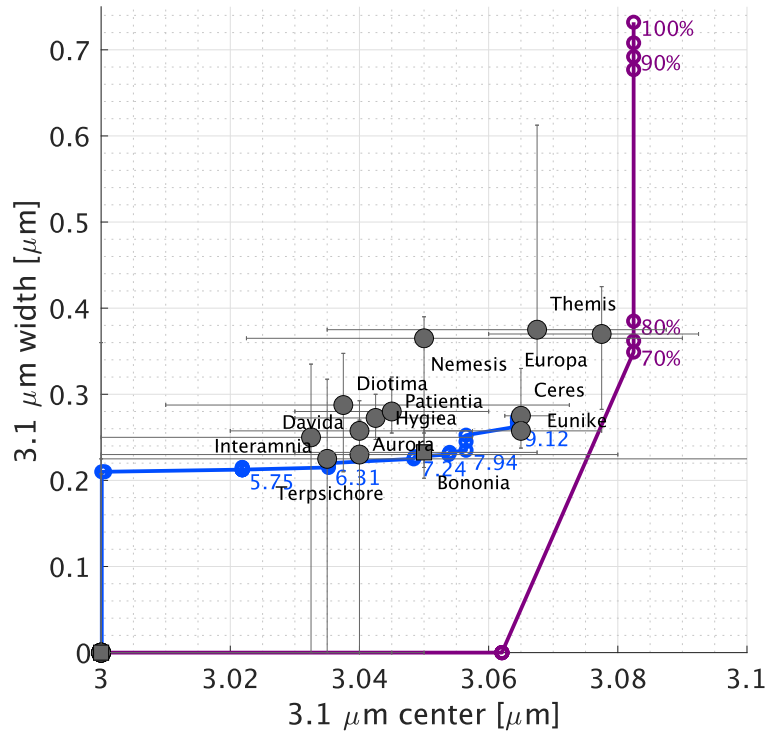


Figure 2. Center and width of the 3.1 μm absorptions for asteroids observed using AKARI (gray circles and squares for C-complex and D- and T-types, respectively) compared to a successive set of mineral assemblages from Case 2 alterations with changing W/R (blue line with W/R values given; 0°C model) and, alternatively, linear mixing fractions of the water-ice coating model (Rivkin & Emery, 2010) with an observed asteroid (2 Pallas) that lacks 3.1 μm absorption (purple line with the values of water-ice coating model fraction given). The 1- σ dispersions are presented by error bars. The values are listed in Supplementary Table 1.

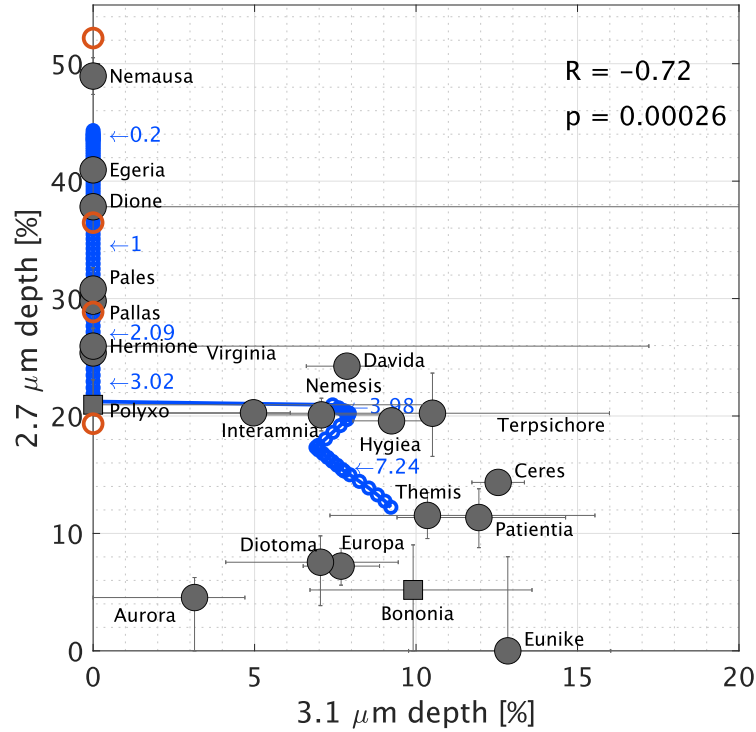


Figure 3. Comparison of absorption features between the model and observations. Data points correspond to C-complex and D- and T-type asteroids observed using AKARI (filled gray circles and squares) and CI and CM carbonaceous chondrites (open orange circles, Supplementary Table 4), respectively. The $1-\sigma$ dispersions are presented by error bars. The values are listed in Supplementary Table 1. The linear correlation coefficient and its significance level are $R = -0.72$ and $p = 0.00026$, both of which support that the two values are (anti-)correlated. The blue line represents Case 2 at 0°C with the changing the initial W/R input (the W/R values are given in the figure). Grain sizes are 0.5 and $100 \mu\text{m}$ for IOM and the other phases, respectively (see Supplementary Figure 11, for the grain size dependence).

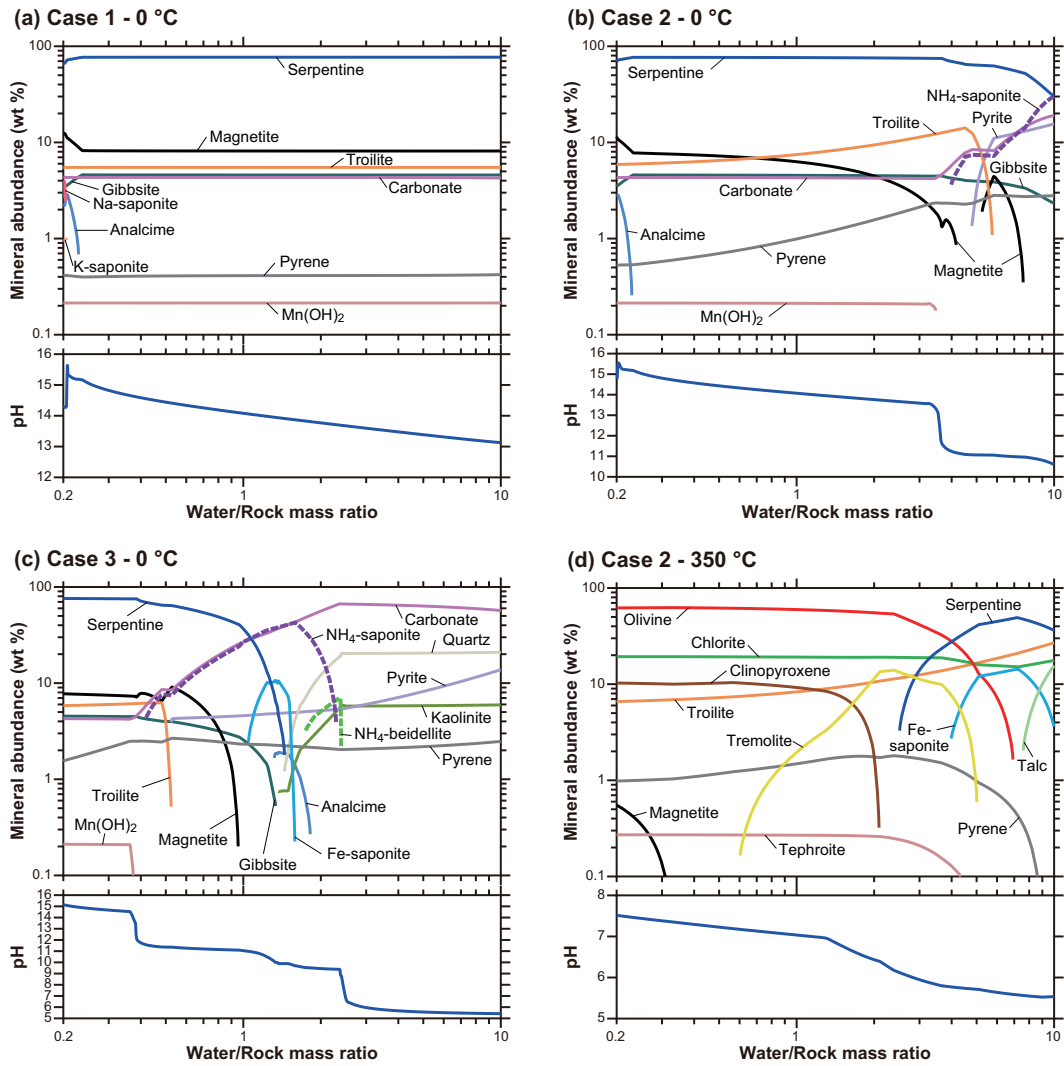


Figure 4. Mineral abundance and pH obtained from thermodynamic modeling as a function of W/R. (a) Case 1, $T = 0^{\circ}\text{C}$. (b) Case 2, $T = 0^{\circ}\text{C}$. (c) Case 3, $T = 0^{\circ}\text{C}$. (d) Case 2, $T = 350^{\circ}\text{C}$.

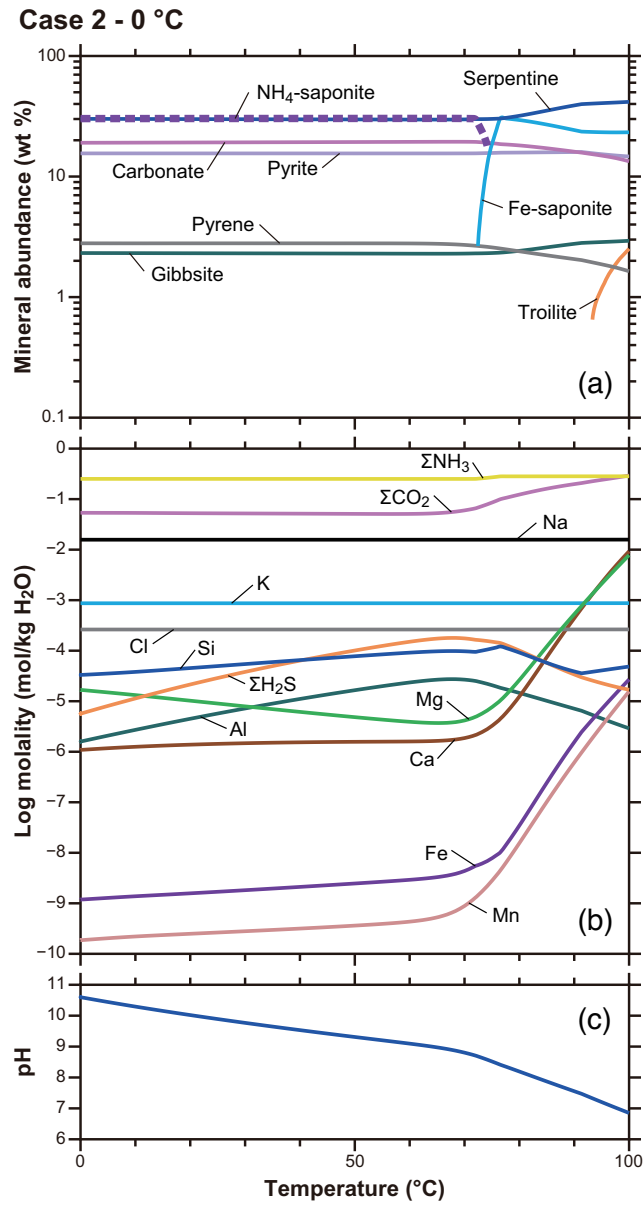


Figure 5. Temperature dependency of (a) abundance of alteration minerals, (b) concentrations of dissolved element and species in fluid, and (c) in-situ pH of fluid at W/R = 10 in Case 2, $T = 0^{\circ}\text{C}$.

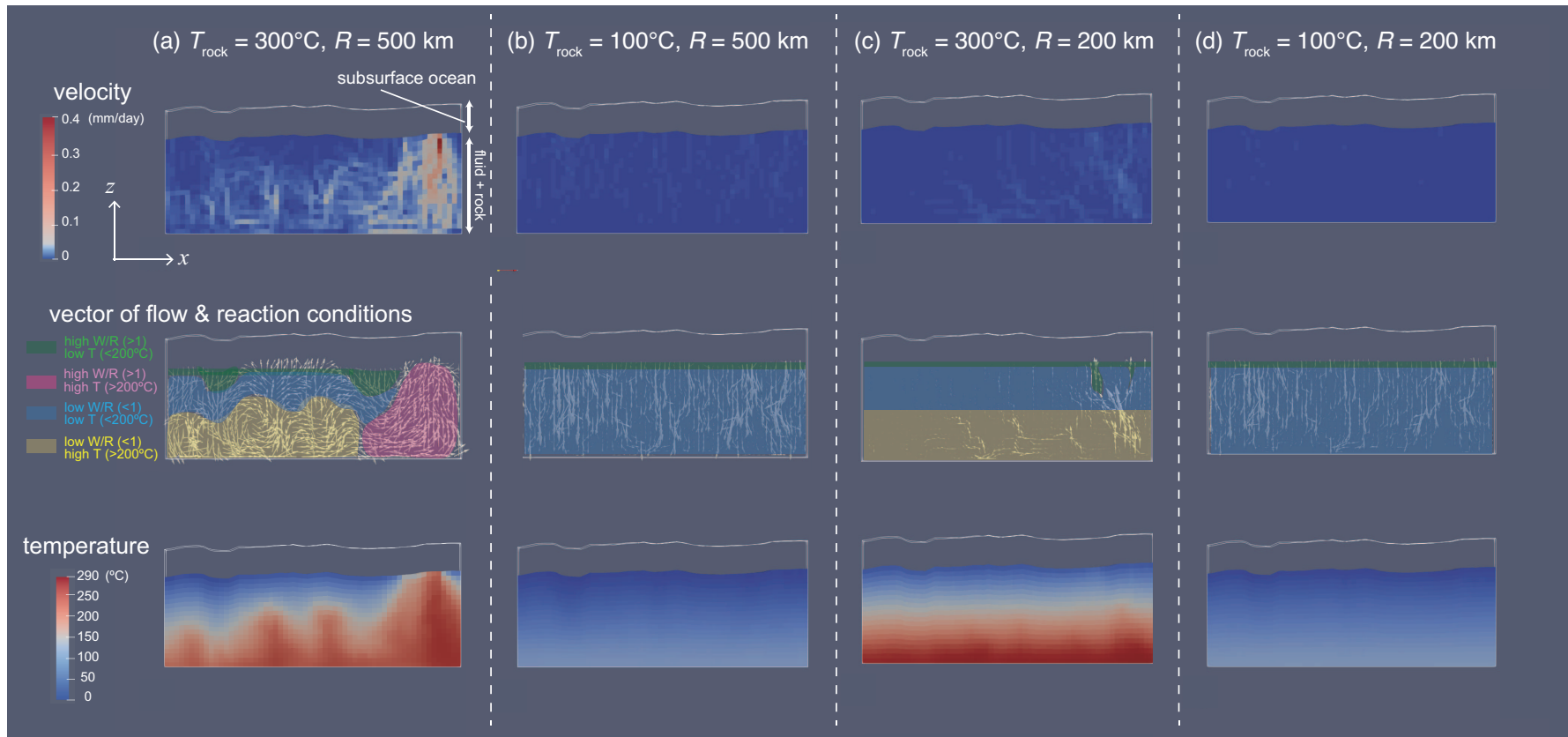


Figure 6. Results of hydrological simulations (snapshot of velocity, vector, and temperature of fluids in each case) for (a) initial core temperature, T_{rock} , = 300°C and planetesimal radius, R , = 500 km, (b) $T_{\text{rock}} = 100^{\circ}\text{C}$ and $R = 500$ km, (c) $T_{\text{rock}} = 300^{\circ}\text{C}$ and $R = 200$ km, and (d) $T_{\text{rock}} = 100^{\circ}\text{C}$ and $R = 200$ km. The white frames represent the calculated area of the two-dimensional grid-block system (total length 240 km and total depth ~ 50 km). The snapshots were taken at 5 Myrs for the 200-km planetesimal and 8 Myrs for the 500-km planetesimal after starting the simulations. The distribution of approximate W/R is indicated in the middle panels. Characteristic minerals expected to form are: NH_4 -saponite and carbonates (high W/R and low T , green), carbonates (high W/R and high T , red), serpentine (low W/R and low T , blue), and unhydrated minerals (high W/R and high T , yellow). See Fig. 4 for details.

Appendix A Text S1. Thermodynamic modeling of the ice mixtures

In order to estimate the volatile loss from icy planetesimals to space via degassing as a consequence of heating by radioactive decay in Stage 1 in Figure 7, we computed the phase change of the ice mixture in a closed system with FREZCHEM (Marion & Kargel, 2007; Marion et al., 2012; Zolotov, 2017). FREZCHEM calculates the chemical equilibrium between dissolved species in the solution, solid phases precipitated from the solution, and gas phases at each temperature and pressure upon freezing with the Gibbs free energy minimization method (Mironenko et al., 1997). As we are interested in gas release upon heating, the solid phases which could form upon freezing (e.g. NH_4CO_3) were suppressed. The equilibrium of gas phases with the solution was controlled by Henry's law. Gas hydrate phases were also considered by extrapolating Henry's law constants below 0°C . We considered the temperature from 25°C to -10°C . A wide pressure range from 1 bar (near the surface) to 1000 bar (the center of a Ceres-sized body) was considered. We assumed a cometary composition (Case 3, Table 1). We neglected H_2S for simplicity.

The abundances of gas, liquid, and solid phases are shown in Supplementary Figure A12. At 1 bar, 95 mol% of CO_2 was in a gas phase regardless of the dominant phase of H_2O . A minor amount of CO_2 was dissolved in the solution as H_2CO_3 , HCO_3^- and CO_3^{2-} . The ratios of HCO_3^- and CO_3^{2-} to H_2CO_3 were controlled by charge balance in the solution, and the neutral pH limited the total abundance of the dissolved CO_2 phases. In contrast, nearly 100 mol% of NH_3 was dissolved in the solution as NH_4^+ . At higher pressure, CO_2 gas hydrate and dissolved phases became dominant CO_2 reservoirs at lower and higher temperature, respectively.

These results suggest that, as temperature increases due to radioactive decay heating, CO_2 ice would melt and be released as CO_2 gas from a near surface layer even before the melting of H_2O ice. Melting of H_2O ice and the subsequent initiation of convection would allow the materials which existed in the deep interior where CO_2 gas hydrate and dissolved phases are stable to once reach the near surface, which led to the release of CO_2 gas. Though the water-rock reactions potentially raise pH and stabilize the dissolved CO_2 phases, the chemical reactions are likely to be slower than the CO_2 phase change and the release of CO_2 gas. As a result, the icy planetesimals, especially their outer parts, would become depleted in CO_2 compared to the original composition whereas NH_3 is retained, modeled as Case 2 (Table 1).

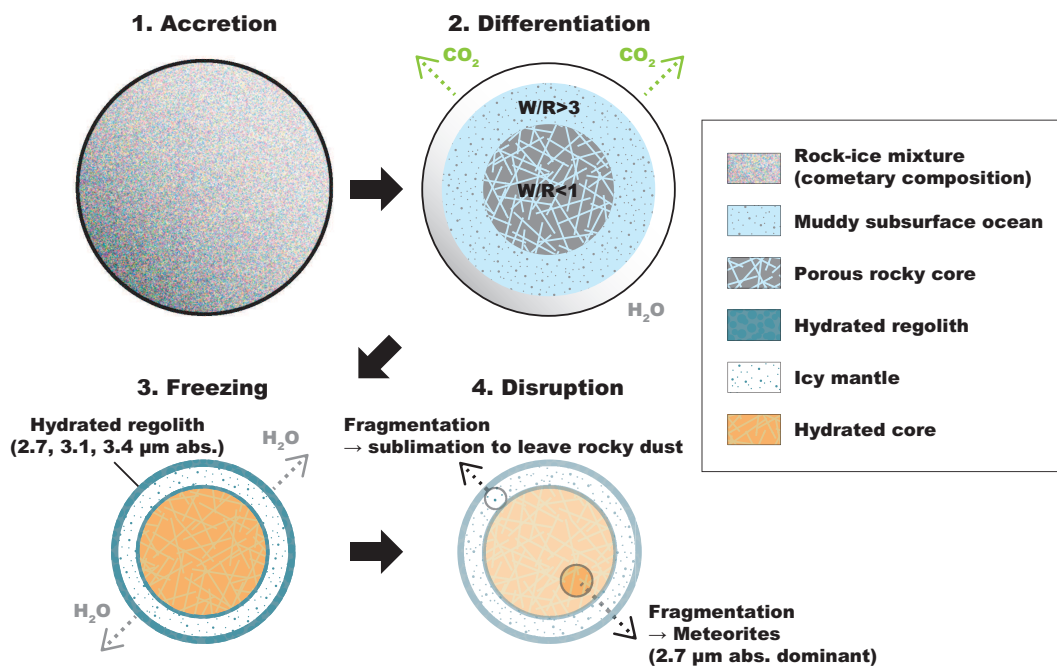


Figure 7. A scenario for the formation and evolution of large C-complex asteroids in the main belt and its relationship to carbonaceous chondrites. Stage 1: Accretion. Stage 2: Differentiation and alteration. Stage 3: Freezing (length depends on the size). Stage 4: Catastrophic disruption.

| Asteroid | $D_{2.7}$ [%] | $D_{3.1}$ [%] | $W_{3.1}$ [μm] | $C_{3.1}$ [μm] |
|--------------------------|------------------------|------------------------|-----------------------------|-----------------------------|
| 0001 Ceres (AKARI) | $14.3^{+0.8}_{-0.8}$ | $12.5^{+0.8}_{-0.8}$ | $0.275^{+0.008}_{-0.008}$ | $3.065^{+0.005}_{-0.003}$ |
| 0001 Ceres (IRTF) | – | $9.35^{+0.16}_{-0.16}$ | $0.304^{+0.004}_{-0.004}$ | $3.047^{+0.004}_{-0}$ |
| 0001 Ceres (Dawn) | $27.3^{+1.5}_{-1.4}$ | $16.0^{+1.7}_{-4.8}$ | $0.283^{+0.018}_{-0.015}$ | $3.065^{+0.008}_{-0.008}$ |
| 0002 Pallas (AKARI) | $29.8^{+0.9}_{-0.9}$ | 0^{+0}_{-0} | 0^{+0}_{-0} | – |
| 0002 Pallas (IRTF) | – | $5.09^{+0.40}_{-0.42}$ | $0.33^{+0.06}_{-0.02}$ | $3.041^{+0.005}_{-0.005}$ |
| 0010 Hygiea (AKARI) | $19.6^{+0.8}_{-0.8}$ | $9.24^{+1.31}_{-1.19}$ | $0.272^{+0.028}_{-0.025}$ | $3.042^{+0.010}_{-0.013}$ |
| 0013 Egeria (AKARI) | $41.0^{+0.9}_{-0.9}$ | 0^{+0}_{-0} | 0^{+0}_{-0} | – |
| 0013 Egeria (IRTF) | – | 0^{+0}_{-0} | 0^{+0}_{-0} | – |
| 0024 Themis (AKARI) | $11.5^{+1.9}_{-2.0}$ | $10.4^{+5.2}_{-3.0}$ | $0.375^{+0.237}_{-0.040}$ | $3.067^{+0.020}_{-0.033}$ |
| 0024 Themis (IRTF) | – | $7.85^{+1.15}_{-1.19}$ | $0.423^{+0.224}_{-0.060}$ | $3.096^{+0.011}_{-0.014}$ |
| 0049 Pales (AKARI) | $30.8^{+1.8}_{-1.9}$ | 0^{+0}_{-0} | 0^{+0}_{-0} | – |
| 0050 Virginia (AKARI) | $25.4^{+3.4}_{-5.0}$ | 0^{+0}_{-0} | 0^{+0}_{-0} | – |
| 0051 Nemausa (AKARI) | $48.9^{+1.6}_{-1.6}$ | 0^{+0}_{-0} | 0^{+0}_{-0} | – |
| 0051 Nemausa (IRTF) | – | 0^{+0}_{-0} | 0^{+0}_{-0} | – |
| 0052 Europa (AKARI) | $7.22^{+1.51}_{-1.62}$ | $7.68^{+1.19}_{-1.17}$ | $0.370^{+0.055}_{-0.088}$ | $3.078^{+0.015}_{-0.018}$ |
| 0052 Europa (IRTF) | – | $4.96^{+0.68}_{-3.05}$ | $0.63^{+0.03}_{-0.34}$ | $3.036^{+0.017}_{-0.010}$ |
| 0081 Terpsichore (AKARI) | $20.2^{+3.4}_{-3.7}$ | $10.5^{+5.5}_{-10.5}$ | $0.225^{+0.093}_{-0.225}$ | $3.035^{+0.123}_{-0.035}$ |
| 0094 Aurora (AKARI) | $4.54^{+1.70}_{-4.54}$ | $3.14^{+1.56}_{-3.14}$ | $0.230^{+0.040}_{-0.230}$ | $3.040^{+0.040}_{-0.040}$ |
| 0106 Dione (AKARI) | $37.8^{+2.2}_{-2.1}$ | $0^{+20.9}_{-0}$ | $0^{+0.208}_{-0}$ | $3^{+0.050}_{-0}$ |
| 0121 Hermione (AKARI) | $25.9^{+1.5}_{-1.5}$ | $0^{+17.2}_{-0}$ | $0^{+0.360}_{-0}$ | $3.000^{+0.040}_{-0}$ |
| 0121 Hermione (IRTF) | – | 0^{+0}_{-0} | 0^{+0}_{-0} | – |
| 0128 Nemesis (AKARI) | $20.1^{+1.4}_{-1.4}$ | $7.07^{+2.03}_{-2.10}$ | $0.365^{+0.025}_{-0.163}$ | $3.050^{+0.040}_{-0.028}$ |
| 0185 Eunike (AKARI) | $0^{+8.02}_{-0}$ | $12.8^{+3.2}_{-3.1}$ | $0.257^{+0.073}_{-0.020}$ | $3.065^{+0.013}_{-0.015}$ |
| 0185 Eunike (IRTF) | – | $3.35^{+3.31}_{-3.35}$ | $0.193^{+0.206}_{-0.193}$ | $3.015^{+0.067}_{-0.016}$ |
| 0308 Polyxo (AKARI) | $21.0^{+2.1}_{-2.4}$ | $0^{+10.5}_{-0}$ | $0^{+0.225}_{-0}$ | $3.000^{+0.045}_{-0}$ |
| 0308 Polyxo (IRTF) | – | 0^{+0}_{-0} | 0^{+0}_{-0} | – |
| 0361 Bononia (AKARI) | $5.19^{+3.84}_{-5.19}$ | $9.91^{+3.68}_{-3.19}$ | $0.232^{+0.023}_{-0.018}$ | $3.05^{+0.018}_{-0.02}$ |
| 0361 Bononia (IRTF) | – | $1.79^{+0.89}_{-1.79}$ | $0.284^{+0.070}_{-0.284}$ | $3.033^{+0.021}_{-0.033}$ |
| 0423 Diotima (AKARI) | $7.55^{+2.25}_{-3.70}$ | $7.04^{+2.41}_{-2.93}$ | $0.288^{+0.060}_{-0.078}$ | $3.038^{+0.035}_{-0.028}$ |
| 0451 Patientia (AKARI) | $11.4^{+2.5}_{-2.6}$ | $11.9^{+2.7}_{-2.5}$ | $0.28^{+0.04}_{-0.03}$ | $3.045^{+0.015}_{-0.015}$ |
| 0451 Patientia (IRTF) | – | $5.04^{+1.96}_{-1.95}$ | $0.281^{+0.091}_{-0.077}$ | $3.033^{+0.031}_{-0.013}$ |
| 0511 Davida (AKARI) | $24.2^{+1.0}_{-0.9}$ | $7.86^{+1.29}_{-1.26}$ | $0.258^{+0.035}_{-0.020}$ | $3.040^{+0.0175}_{-0.020}$ |
| 0511 Davida (IRTF) | – | 0^{+0}_{-0} | 0^{+0}_{-0} | – |
| 0704 Interamnia (AKARI) | $20.3^{+0.9}_{-0.9}$ | $4.97^{+1.14}_{-4.97}$ | $0.25^{+0.09}_{-0.25}$ | $3.033^{+0.025}_{-0.033}$ |
| 0704 Interamnia (IRTF) | – | $2.73^{+1.18}_{-1.07}$ | $0.302^{+0.082}_{-0.178}$ | $3.030^{+0.013}_{-0.011}$ |

Table A1. 2.7 μm absorption depth ($D_{2.7}$), 3.1 μm absorption depth ($D_{3.1}$), width ($W_{3.1}$), and center ($C_{3.1}$) of asteroids spectra acquired using AKARI, IRTF, and Dawn. Median and 68% confidence intervals are shown.

| Endmember | RELAB ID or reference | n |
|---------------------------|--|------------------|
| Alabandite | WV-JWH-005 (BKR1WV005) | 2.73 |
| Analcime | USGS, GDS1 | 1.495 |
| NH ₄ -saponite | Ehlmann et al.(Ehlmann et al., 2018) | 1.56 |
| Andradite | GN-EAC-004 (LAGN04) | 1.77 |
| Beidellite | BE-EAC-003 (LABE03) | 1.46 |
| Brucite | JB-JLB-944-A (BKR1JB944A) | 1.58 |
| Calcite | CB-EAC-010-A (LACB10A) | 1.57 |
| Chrysotile | CR-TXH-006 (LACR06) | 1.57 |
| Clinochlore | CL-TXH-014 (LACL14) | 1.59 |
| Diaspore | HO-EAC-007-A (LAHO07A) | 1.495 |
| Diopside | DD-MDD-074 (BKR1DD074) | 1.7 |
| Fayalite | DD-MDD-098 (BKR1DD098) | 1.875 |
| Ferrosaponite | JB-JLB-761-A (BKR1JB761A) | 1.58 |
| Forsterite | DD-MDD-085 (BKR1DD085) | 1.665 |
| Gibbsite | HO-EAC-004-A (LAHO04A) | 1.6 |
| Greenalite | GR-EAC-011-A (BKR1GR011A) | 1.685 |
| Grossular | USGS, WS485 | 1.745 |
| Hedenbergite | DL-CMP-082-A (BKR1DL082A) | 1.735 |
| H ₂ O ice | Mastrapa et al.(Mastrapa et al., 2009) | given |
| IOM | Kaplan et al.(Kaplan et al., 2018) | – ^a |
| Kaolinite | KA-EAC-001 (LAKA01) | 1.59 |
| Laumontite | ZE-EAC-019 (LAZE19) | 1.525 |
| Magnesite | JB-JLB-946 (BKR1JB946A) | 1.615 |
| Magnetite | MG-EAC-002 (LAMG02) | 2.0 ^b |
| Minnesotaitite | MN-EAC-001-A (BKR1MN001A) | 1.62 |
| Muscovite | SR-JFM-071-A (BKR1SR071A) | 1.595 |
| Pyrite | SC-EAC-119 (LASC119) | 5.0 ^c |
| Quartz | JB-CMP-150 (995F150) | 1.545 |
| Rhodochrosite | CB-EAC-068-A (BKR1CB068A) | 1.75 |
| Saponite | SA-TXH-055 (LASA55) | 1.56 |
| Siderite | CB-EAC-008-A (LACB08A) | 1.77 |
| Talc | EA-EAC-015 (BKR1EA015) | 1.585 |
| Troilite | EA-EAC-001-B (LAEA01B) | 4.0 ^d |

Table A2. References for endmember reflectances and refractive indices. Sample IDs are those in RELAB unless otherwise stated. The real part of refractive index n is from <https://refractiveindex.info/> unless otherwise stated. a: Measured reflectance is used. b: Glotch and Rossman (2009), c: K. Sato (1984), d: Pollack et al. (1994).

| Phase | Abundance [wt.%] |
|--------------------------------|------------------|
| SiO ₂ | 36.314 |
| Al ₂ O ₃ | 3.598 |
| FeO | 5.163 |
| MnO | 0.204 |
| MgO | 26.164 |
| CaO | 2.893 |
| Na ₂ O | 0.484 |
| K ₂ O | 0.041 |
| FeS | 6.563 |
| Fe metal | 17.388 |
| Pyrene | 1.116 |
| HCl | 0.010 |
| HCN | 0.063 |
| Total | 100 |

Table A3. Initial bulk rock composition for geochemical modeling. A mean composition of CV chondrites was assumed (Pearson et al., 2006; Henderson et al., 2009; Clay et al., 2017). S, Cl, N, and C were included as FeS, HCl, HCN, and pyrene plus HCN, respectively. The abundances of FeO and Fe metal were scaled to result in $\text{MgO}/(\text{MgO}+\text{FeO}) = 0.9$.

| Meteorite | ID or reference |
|-----------------------------|------------------------|
| Murchison (heated at 600°C) | MT-JMS-190 (BKR1MT190) |
| Cold Bokkeveld | Ehlmann et al. (2018) |
| | MT-JMS-186 (BKR1MT186) |
| Tagish Lake | MT-MEZ-011 (LCMT11) |
| | MT-MEZ-012 (LCMT12) |
| Ivuna (heated at 100°C) | MP-TXH-018-F (LAMP18F) |

Table A4. References for meteorites reflectance spectra. IDs are those in RELAB. Spectral data were selected and combined as reported in Kurokawa et al. (2020).

| Name | Classification | Diameter [km] | Albedo | Semi-major axis [au] | Family | 3.1 μm abs. |
|----------------|----------------|---------------|--------|----------------------|--------|------------------------|
| 1 Ceres | C | 973.9 | 0.087 | 2.767 | – | A |
| 2 Pallas | B | 512.6 | 0.150 | 2.772 | F | – |
| 10 Hygiea | C | 428.5 | 0.066 | 3.141 | F | A |
| 13 Egeria | Ch | 203.4 | 0.086 | 2.578 | – | – |
| 24 Themis | C | 176.8 | 0.084 | 3.137 | F | W |
| 49 Pales | Ch | 148.0 | 0.061 | 3.103 | – | – |
| 50 Virginia | Ch | 84.4 | 0.050 | 2.649 | – | – |
| 51 Nemausa | Cgh | 147.2 | 0.094 | 2.366 | – | – |
| 52 Europa | C | 350.4 | 0.043 | 3.093 | – | A/W |
| 81 Terpsichore | C | 123.0 | 0.048 | 2.853 | F | A? |
| 94 Aurora | C | 179.2 | 0.053 | 3.156 | – | A? |
| 106 Dione | Cgh | 153.4 | 0.084 | 3.180 | – | – |
| 121 Hermione | Ch | 194.1 | 0.058 | 3.448 | – | – |
| 128 Nemesis | C | 177.9 | 0.059 | 2.750 | F | A/W |
| 185 Eunike | C | 167.7 | 0.057 | 2.737 | – | A |
| 308 Polyxo | T | 135.2 | 0.052 | 2.749 | – | – |
| 361 Bononia | D | 151.8 | 0.040 | 3.957 | – | A |
| 423 Diotima | C | 226.9 | 0.049 | 3.067 | I | A |
| 451 Patientia | C | 234.9 | 0.071 | 3.061 | – | A |
| 511 Davida | C | 291.0 | 0.070 | 3.164 | – | A |
| 704 Interamnia | Cb | 316.2 | 0.075 | 3.059 | – | A? |

Table A5. A summary of asteroid properties. Classification: Bus-DeMeo taxonomy as summarized by Hasegawa et al. (2017). Diameter, albedo, and semi-major axis: Data as summarized in (Usui et al., 2019). Family: F (having a family), – (not having a family), or I (interloper), as summarized by Usui et al. (2019); Vernazza et al. (2021). 3.1 μm absorption: A (ammoniated phyllosilicate), W (water ice), A/W (ammoniated phyllosilicates and/or water ice), and – (non-detection). Possible detection (band depths are nonzero at their median values but 1- σ error bars range to zero) is denoted by “?” at the end.

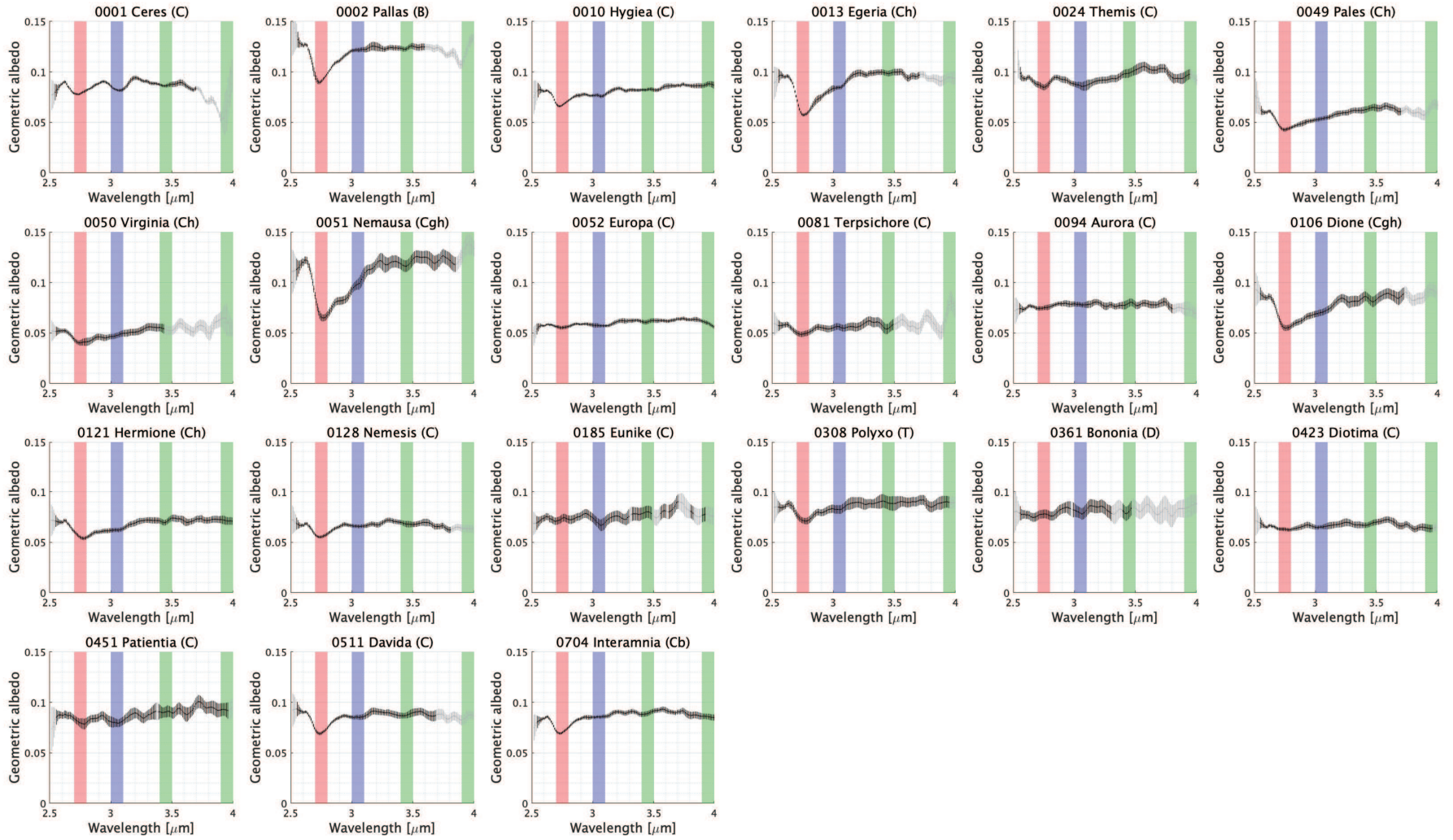


Figure A1. Reflectance spectra of the C-complex and D- and T-type asteroids observed by AKARI infrared space telescope. Data are from Usui et al. (2019). The gray data points indicate the unreliable wavelength regions due to large uncertainties ($> 10\%$) defined by Usui et al. (2019). We highlighted the positions of absorption features: $2.7 \mu\text{m}$ (hydrous minerals, red), $3.1 \mu\text{m}$ (ammoniated saponite, blue), and 3.4 and $4.0 \mu\text{m}$ (carbonates, green).

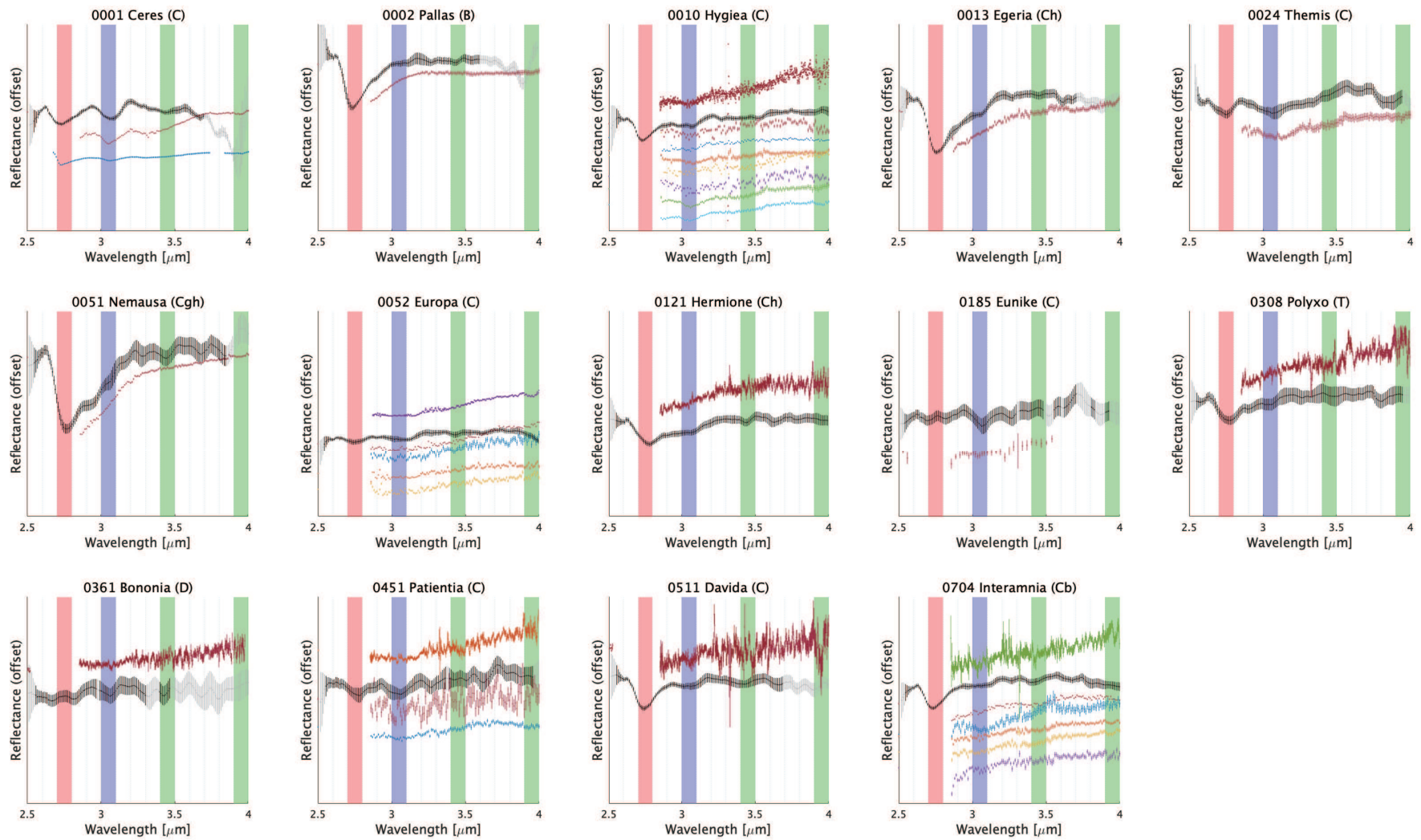


Figure A2. Comparison of reflectance spectra acquired using AKARI (black points), IRTF (colored points), and Dawn (blue points for Ceres).

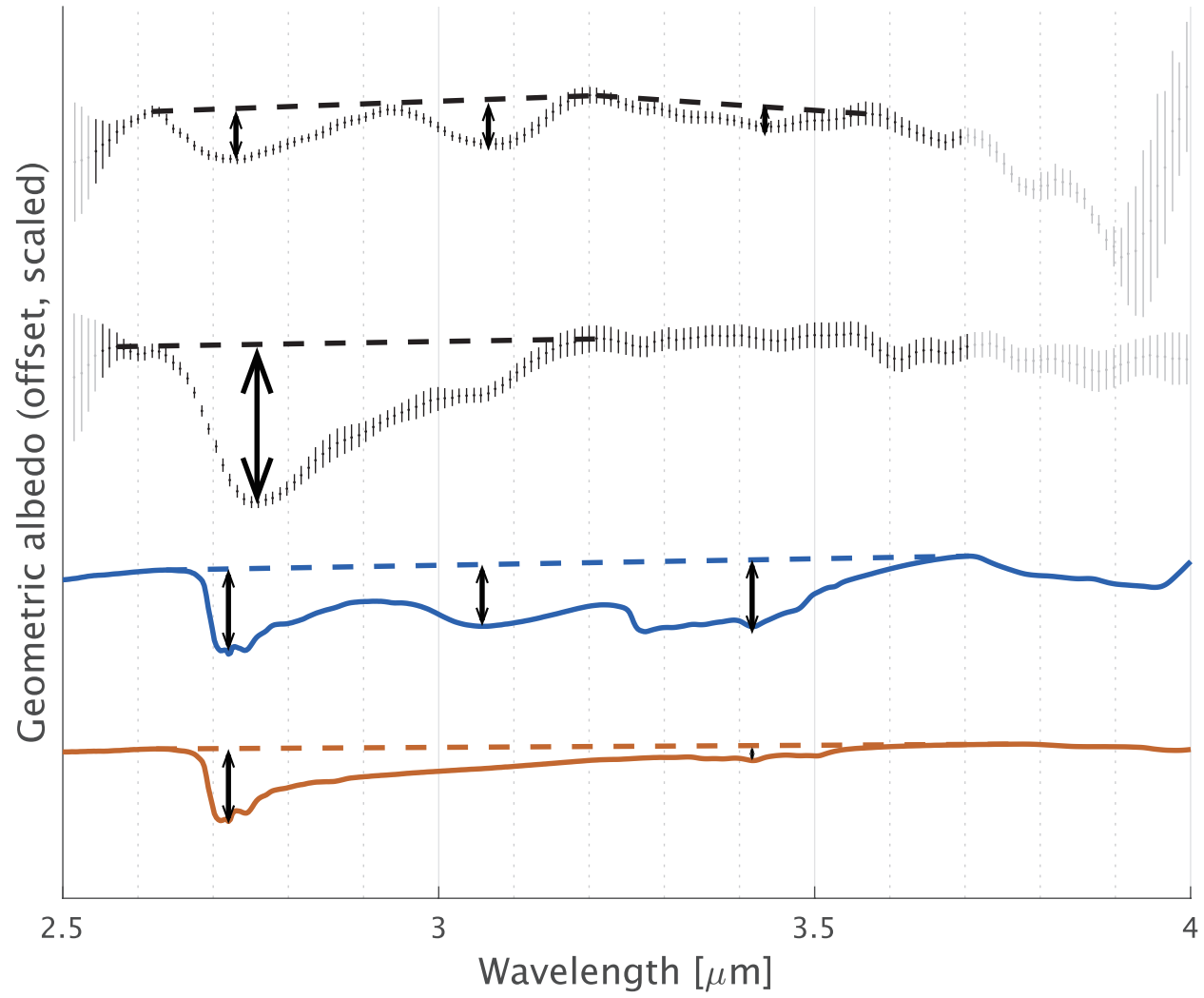


Figure A3. Definition of the absorption band depth. Black arrows indicate $R_c - R_\lambda$.

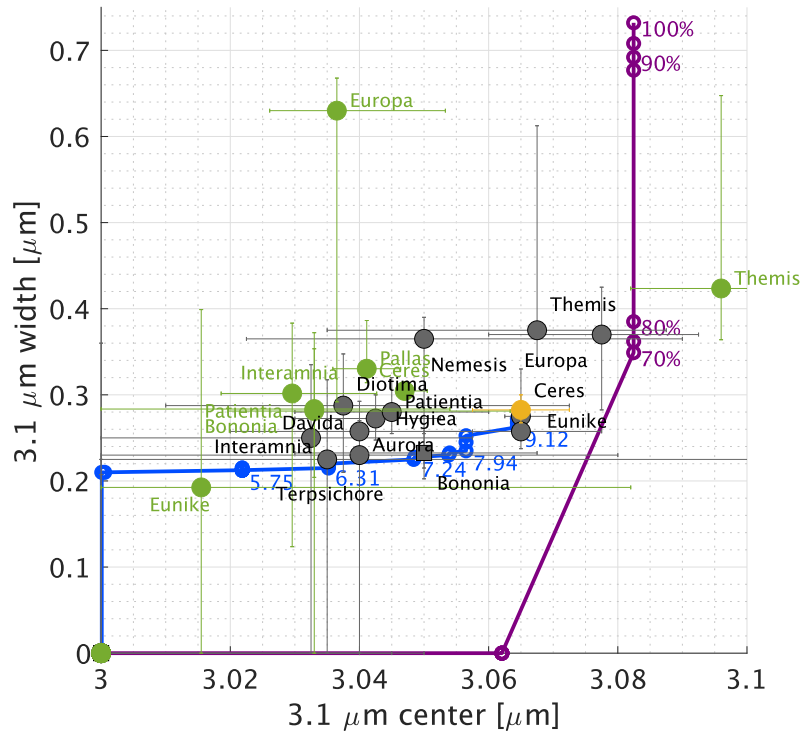


Figure A4. Center and width of the observed $3.1 \mu\text{m}$ absorptions for asteroids observed by AKARI (gray), IRTF (green), and Dawn for Ceres (yellow). Model lines are the same with those in Figure 2 in the main text.

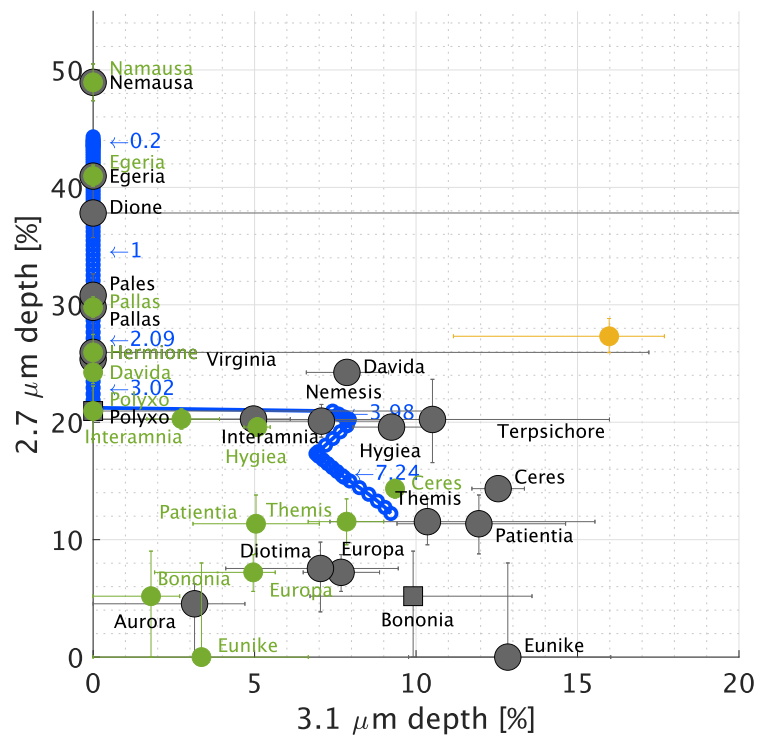


Figure A5. Absorption depths for asteroids observed by AKARI (gray), IRTF (green), and Dawn for Ceres (yellow). Model line is the same with that in Figure 3 in the main text.

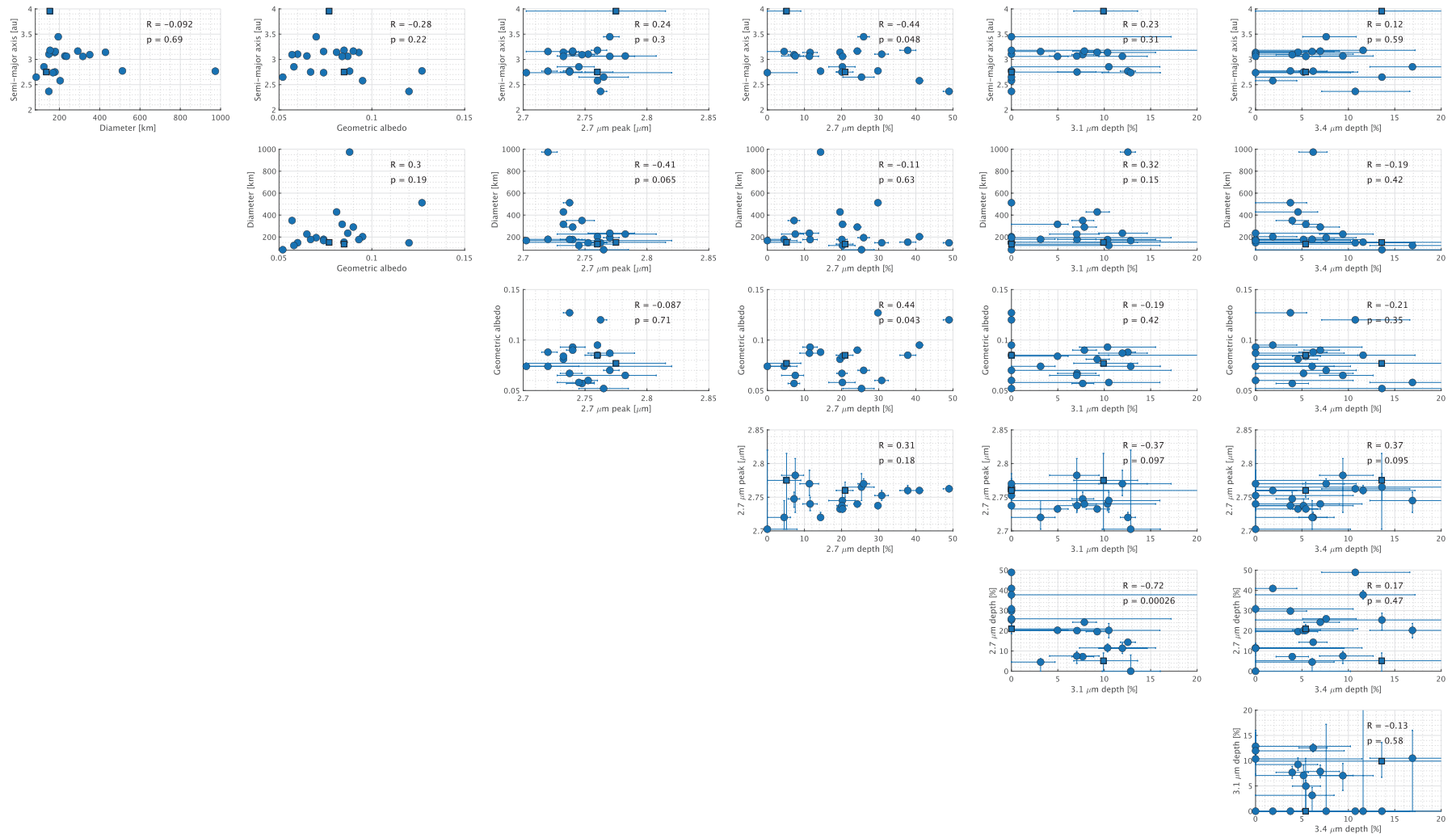


Figure A6. Correlation plot for the properties of C-complex (circle) and D- and T-type (square) asteroids observed by AKARI. The linear-correlation coefficient R is given in each panel.

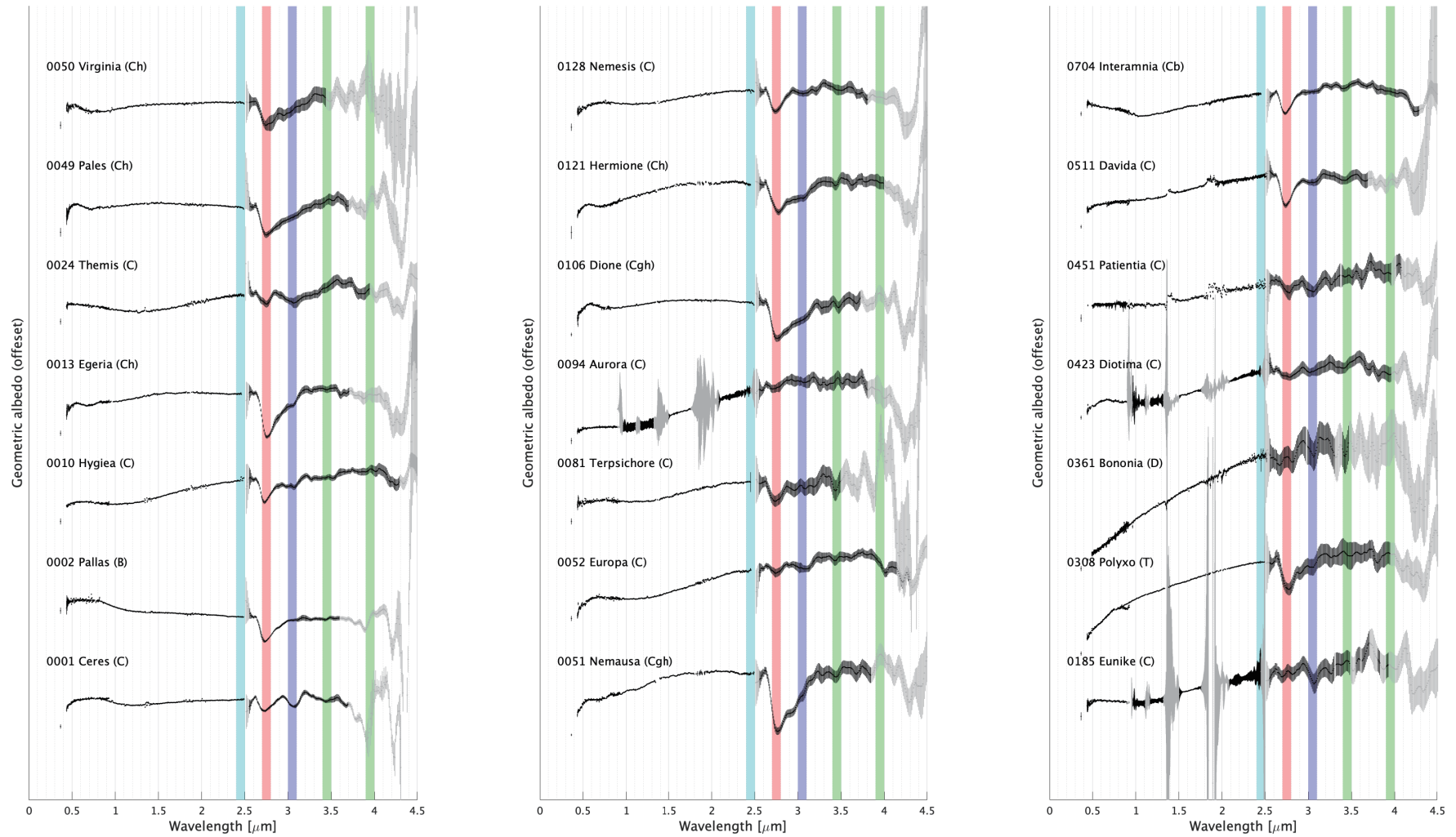


Figure A7. Combined spectra from visible to infrared wavelengths acquired using AKARI (Usui et al., 2019) and ground-based observations (Bus & Binzel, 2002; DeMeo et al., 2009; Takir & Emery, 2012). Data were compiled by Hasegawa et al. (2017). The gray data points indicate the unreliable wavelength region due to large uncertainties ($> 10\%$) defined by Usui et al. (2019). We highlighted the positions of absorption features: $2.7 \mu\text{m}$ (hydrrous minerals, red), $3.1 \mu\text{m}$ (ammoniated saponite, blue), 3.4 and $4.0 \mu\text{m}$ (carbonates, green), and $2.45 \mu\text{m}$ (brucite, cyan).

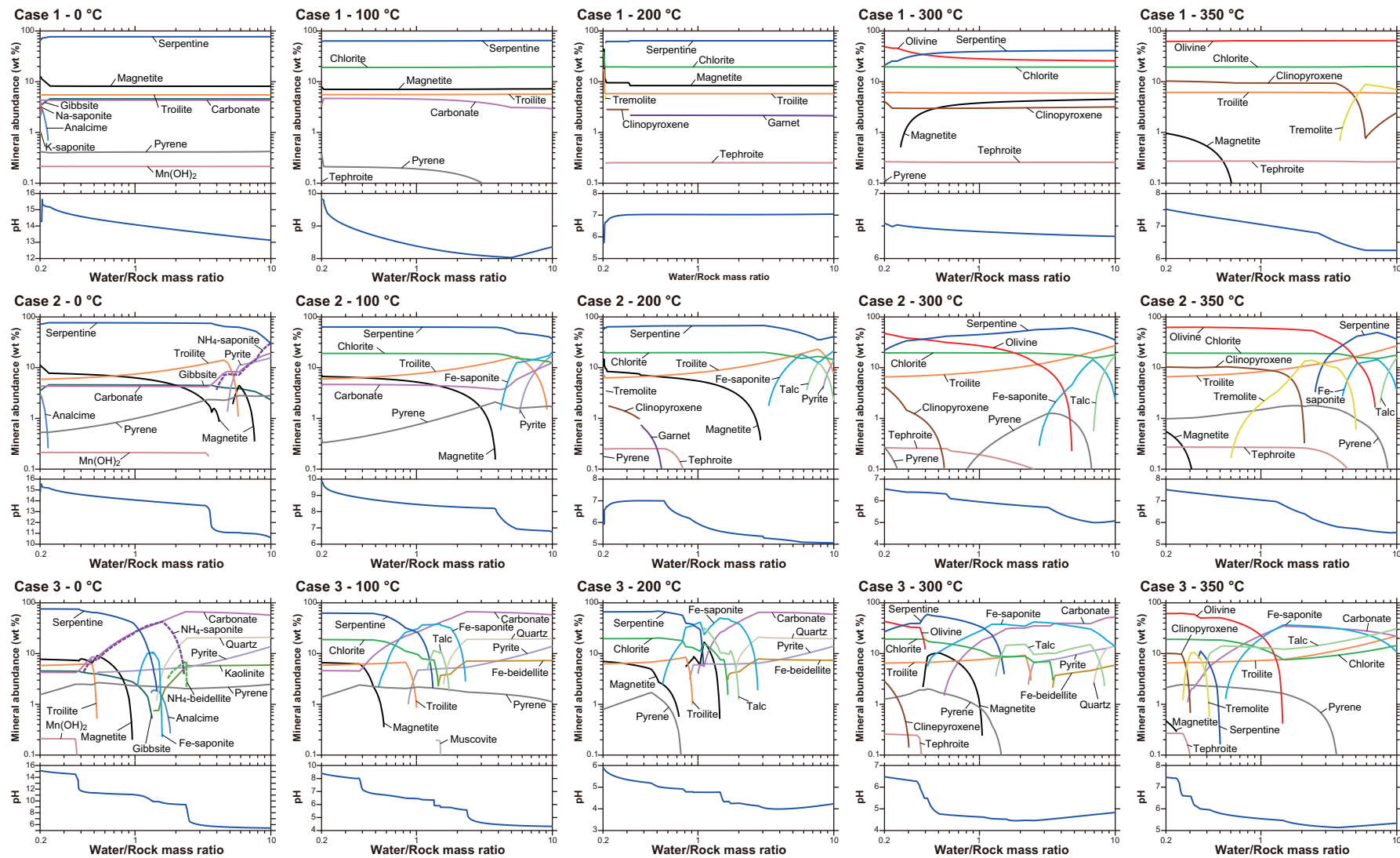


Figure A8. Mineral abundance and pH obtained from thermodynamic modeling as a function of W/R in Case 1-3 (rows from top to bottom) for $T = 0, 100, 200, 300,$ and 350 °C (columns from left to right).

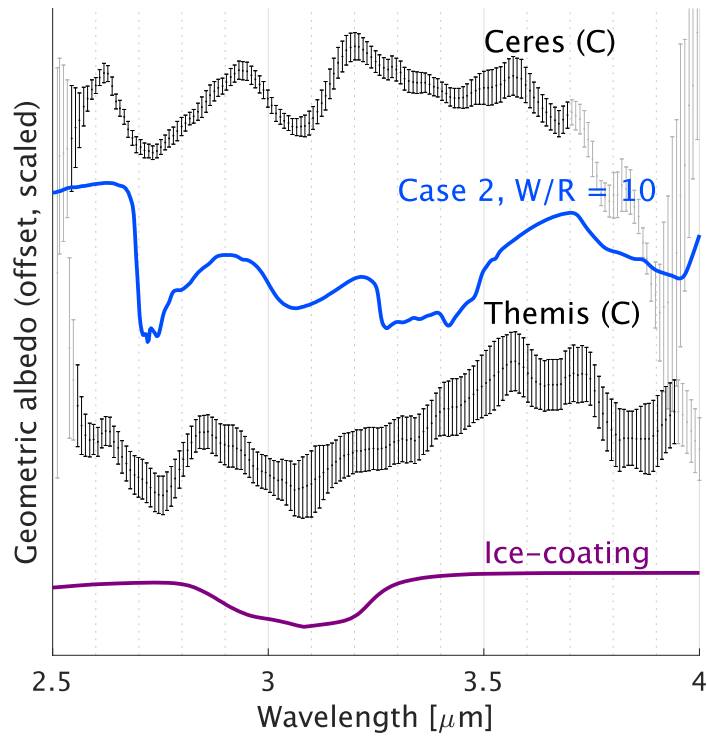


Figure A9. Comparison of asteroid spectra acquired using AKARI, Case 2 of our alteration model that we proposed creates asteroids with NH_4 -bearing phyllosilicates, and the water-ice coating model of Rivkin and Emery (2010). While 24 Themis is consistent with the water-ice coating model, 1 Ceres resembles the model with NH_4 -bearing phyllosilicates.

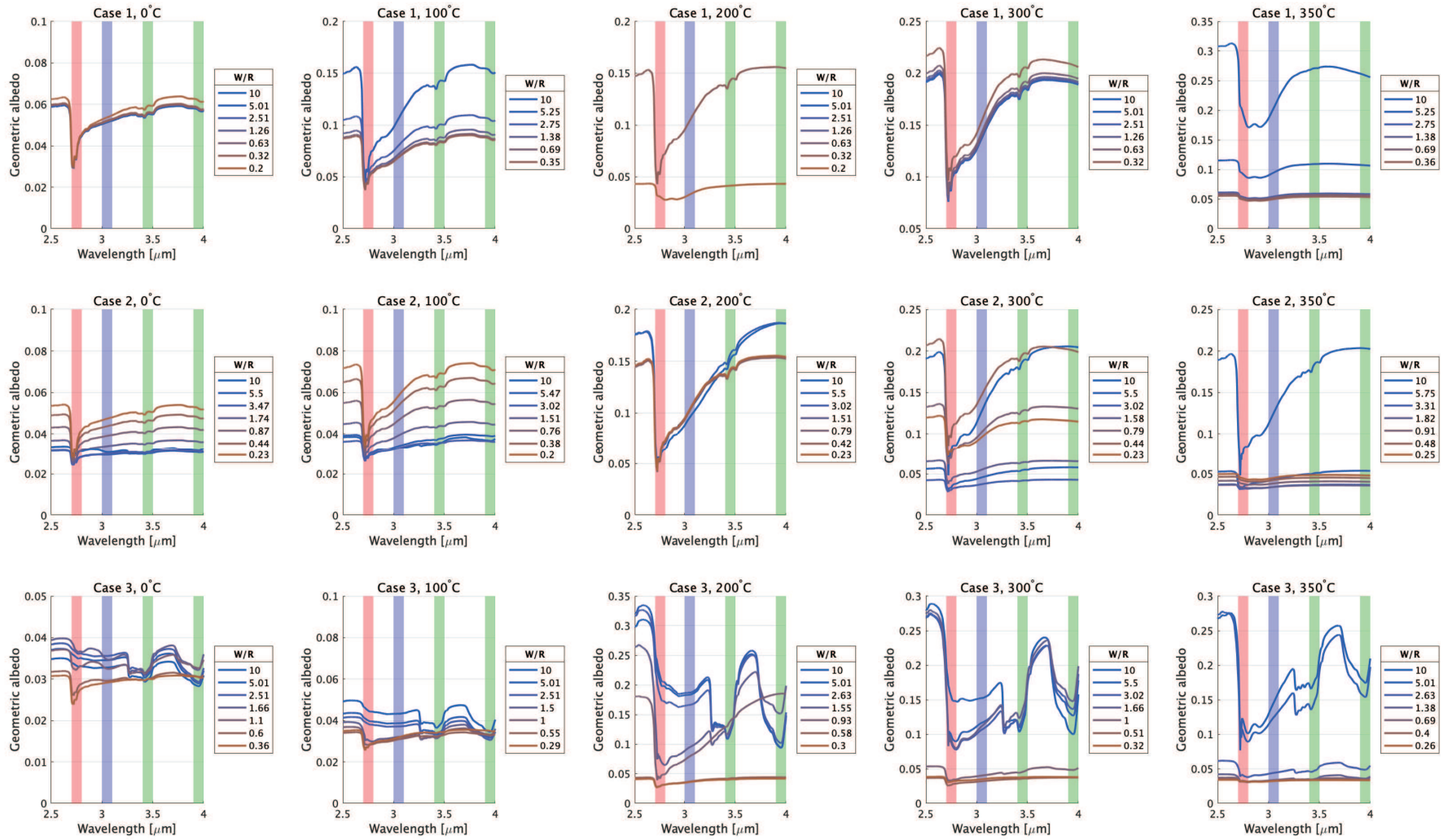


Figure A10. Model infrared reflectance spectra for various W/R in Case 1–3 (columns from left to right) and $T = 0, 100, 200, 300,$ and 350°C (rows from top to bottom). We highlighted the positions of absorption features: $2.7 \mu\text{m}$ (hydrrous minerals, red), $3.1 \mu\text{m}$ (ammoniated saponite, blue), and 3.4 and $4.0 \mu\text{m}$ (carbonates, green).

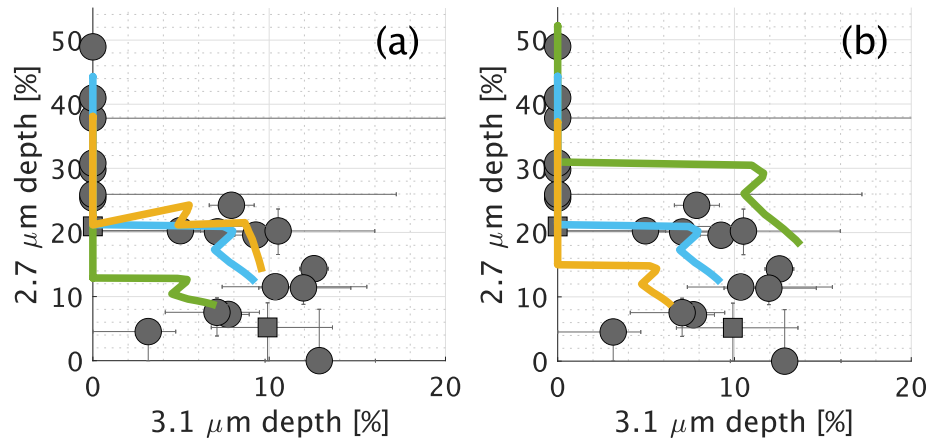


Figure A11. Dependence of modeled absorption band depths on grain sizes. (a) $d = 0.5 \mu\text{m}$ for IOM and $d = 200$ (green), 100 (cyan), and $50 \mu\text{m}$ (yellow) for the other minerals. (b) $d = 100 \mu\text{m}$ for the other minerals and $d = 1$ (green), 0.5 (cyan), and $0.3 \mu\text{m}$ (yellow) for IOM. Data points are the same with Figure 3 in the main text.

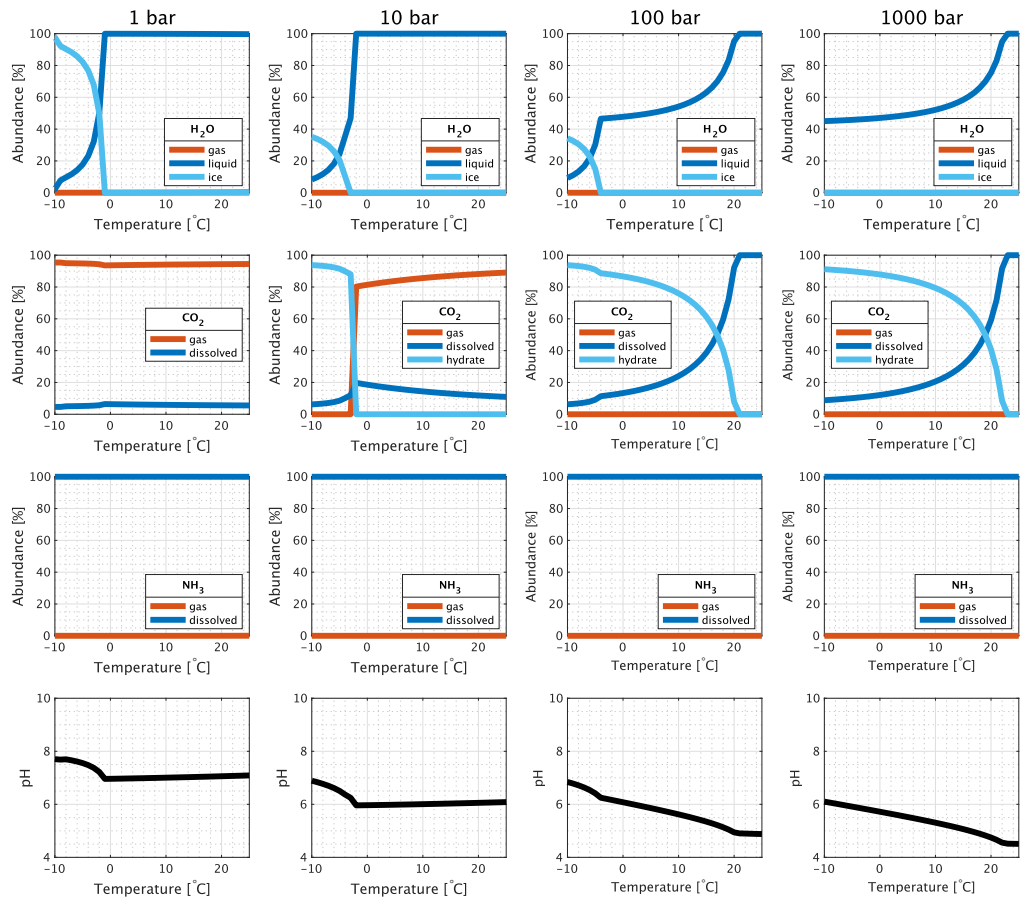


Figure A12. Abundances of gas, liquid, and solid phases for H₂O, CO₂, and NH₃ (rows from top to bottom) at 1, 10, 100, 1000 bar (columns from left to right) obtained from the thermodynamic calculations for the ice mixtures.

Acknowledgments

The data that support the plots presented in this paper are available at <https://doi.org/10.6084/m9.figshare.14338760.v1>. AKARI data are available at <http://www.ir.isas.jaxa.jp/AKARI/Archive/>. EQ3/6 was developed by Wolery and Jarek (2003). The code is available from Lawrence Livermore National Laboratory (LLNL). GETFLOWS is a commercially-available hydrological simulator and is the property of Gesphere Environmental Technology Corp. FREZCHEM is an open source code developed by Marion et al. (2012). The code is available from G. Marion. We thank the editor Francis Nimmo, Lucy F. Lim, and three anonymous reviewers for their careful review and constructive comments, which highly improved our manuscript. We thank Andrew Rivkin, Driss Takir, Valerie Fox, and Hannah Kaplan for sharing reflectance data, Takehiro Hiroi and Moe Matsuoka for discussion about infrared reflectance spectra of meteorites, Mikhail Zolotov for sharing the modified version of the FREZCHEM code, and Keisuke Fukushi for providing thermodynamic parameters for smectites. This study was supported by JSPS KAKENHI Grant number 15K05277, 17H01175, 17H06454, 17H06455, 17H06456, 17H06457, 17H06458, 17H06459, 17K05636, 18K13602, 19H00725, 19H01960, 19H05072, 20KK0080, 21H04514, 21K13976, and JSPS Core-to-Core Program "International Network of Planetary Sciences." Part of the data utilized in this publication were obtained and made available by the MITH-NEOS MIT-Hawaii Near-Earth Object Spectroscopic Survey. The IRTF is operated by the University of Hawaii under Cooperative Agreement no. NCC 5-538 with the National Aeronautics and Space Administration, Office of Space Science, Planetary Astronomy Program. The MIT component of this work is supported by NASA grant 09-NEOO009-0001, and by the National Science Foundation under Grants Nos. 0506716 and 0907766.

References

- Alexander, C. M. O. (2019). Quantitative models for the elemental and isotopic fractionations in chondrites: The carbonaceous chondrites. *Geochimica et Cosmochimica Acta*, *254*, 277–309.
- Alexander, C. M. O., Bowden, R., Fogel, M. L., Howard, K. T., Herd, C. D. K., & Nittler, L. R. (2012). The provenances of asteroids, and their contributions to the volatile inventories of the terrestrial planets. *Science*, *337*(6095), 721–723.
- Alexander, C. M. O., Cody, G. D., De Gregorio, B. T., Nittler, L. R., & Stroud, R. M. (2017). The nature, origin and modification of insoluble organic matter in chondrites, the major source of earth's c and n. *Geochemistry*, *77*(2), 227–256.
- Andrews, S. M., Huang, J., Pérez, L. M., Isella, A., Dullemond, C. P., Kurtovic, N. T., . . . others (2018). The disk substructures at high angular resolution project (DSHARP). I. Motivation, sample, calibration, and overview. *The Astrophysical Journal Letters*, *869*(2), L41.
- Beck, P., Quirico, E., Sevestre, D., Montes-Hernandez, G., Pommerol, A., & Schmitt, B. (2011). Goethite as an alternative origin of the 3.1 μm band on dark asteroids. *Astronomy & Astrophysics*, *526*, A85.
- Beitz, E., Blum, J., Parisi, M. G., & Trigo-Rodríguez, J. (2016). The collisional evolution of undifferentiated asteroids and the formation of chondritic meteoroids. *The Astrophysical Journal*, *824*(1), 12.
- Bischoff, A., Scott, E. R., Metzler, K., & Goodrich, C. A. (2006). Nature and origins of meteoritic breccias. *Meteorites and the early solar system II*, 679–712.
- Bland, P. A., Jackson, M. D., Coker, R. F., Cohen, B. A., Webber, J. B. W., Lee, M. R., . . . others (2009). Why aqueous alteration in asteroids was isochemical: High porosity \neq high permeability. *Earth and Planetary Science Letters*, *287*(3-4), 559–568.
- Bland, P. A., & Travis, B. J. (2017). Giant convecting mud balls of the early solar system. *Science Advances*, *3*(7), e1602514.
- Blum, J., Schröpler, R., Davidsson, B. J., & Trigo-Rodríguez, J. M. (2006). The

- physics of protoplanetary dust agglomerates. I. Mechanical properties and relations to primitive bodies in the solar system. *The Astrophysical Journal*, *652*(2), 1768.
- Bockelée-Morvan, D., & Biver, N. (2017). The composition of cometary ices. *Philosophical Transactions of the Royal Society A: Mathematical, Physical and Engineering Sciences*, *375*(2097), 20160252.
- Bottke, W. F., Broz, M., O'Brien, D. P., Bagatin, A. C., Morbidelli, A., & Marchi, S. (2015). The collisional evolution of the main asteroid belt. *Asteroids IV*, *1*, 701–724.
- Bottke, W. F., Durda, D. D., Nesvorný, D., Jedicke, R., Morbidelli, A., Vokrouhlický, D., & Levison, H. (2005). The fossilized size distribution of the main asteroid belt. *Icarus*, *175*(1), 111–140.
- Brasser, R., & Mojzsis, S. J. (2020). The partitioning of the inner and outer Solar System by a structured protoplanetary disk. *Nature Astronomy*, *4*(5), 492–499.
- Brearley, A. J. (2006). The action of water. *Meteorites and the early solar system II*, *943*, 587–624.
- Brown, M. E. (2016). The 3–4 μm spectra of Jupiter Trojan asteroids. *The Astronomical Journal*, *152*(6), 159.
- Burbine, T. H. (1998). Could G-class asteroids be the parent bodies of the CM chondrites? *Meteoritics & Planetary Science*, *33*(2), 253–258.
- Burbine, T. H., & Greenwood, R. C. (2020). Exploring the bimodal Solar System via sample return from the main asteroid belt: The case for revisiting Ceres. *Space science reviews*, *216*(4), 1–27.
- Bus, S. J., & Binzel, R. P. (2002). Phase II of the small main-belt asteroid spectroscopic survey: The observations. *Icarus*, *158*(1), 106–145.
- Buseck, P. R., & Hua, X. (1993). Matrices of carbonaceous chondrite meteorites. *Annual Review of Earth and Planetary Sciences*, *21*(1), 255–305.
- Campins, H., Hargrove, K., Pinilla-Alonso, N., Howell, E. S., Kelley, M. S., Licandro, J., ... Ziffer, J. (2010). Water ice and organics on the surface of the asteroid 24 Themis. *Nature*, *464*(7293), 1320–1321.
- Castillo-Rogez, J., Brophy, J., Miller, K., Sori, M., Scully, J., Quick, L., ... Zacny, K. (in press). Concepts for the future exploration of dwarf planet Ceres' habitability. *The Planetary Science Journal*.
- Castillo-Rogez, J., Neveu, M., McSween, H. Y., Fu, R. R., Toplis, M. J., & Prettyman, T. (2018). Insights into Ceres's evolution from surface composition. *Meteoritics & Planetary Science*, *53*(9), 1820–1843.
- Castillo-Rogez, J. C., & McCord, T. B. (2010). Ceres' evolution and present state constrained by shape data. *Icarus*, *205*(2), 443–459.
- Chan, Q. H., Zolensky, M. E., Kebukawa, Y., Fries, M., Ito, M., Steele, A., ... others (2018). Organic matter in extraterrestrial water-bearing salt crystals. *Science Advances*, *4*(1), eaao3521.
- Charnoz, S., Avice, G., Hyodo, R., Pignatale, F. C., & Chaussidon, M. (2021). Forming pressure traps at the snow line to isolate isotopic reservoirs in the absence of a planet. *Astronomy & Astrophysics*, *652*, A35.
- Ciarniello, M., De Sanctis, M. C., Ammannito, E., Raponi, A., Longobardo, A., Palomba, E., ... others (2017). Spectrophotometric properties of dwarf planet Ceres from the VIR spectrometer on board the Dawn mission. *Astronomy & Astrophysics*, *598*, A130.
- Clay, P. L., Burgess, R., Busemann, H., Ruzié-Hamilton, L., Joachim, B., Day, J. M., & Ballentine, C. J. (2017). Halogens in chondritic meteorites and terrestrial accretion. *Nature*, *551*(7682), 614–618.
- Cohen, B. A., & Coker, R. F. (2000). Modeling of liquid water on CM meteorite parent bodies and implications for amino acid racemization. *Icarus*, *145*(2), 369–381.

- Coker, R. F., & Cohen, B. A. (2001). The effect of liquid transport on the modeling of CM parent bodies. *Meteoritics and Planetary Science Supplement*, *36*, A43.
- Consolmagno, G. J., Britt, D. T., & Macke, R. J. (2008). The significance of meteorite density and porosity. *Geochemistry*, *68*(1), 1–29.
- Dasgupta, R., & Grewal, D. S. (2019). Origin and early differentiation of carbon and associated life-essential volatile elements on Earth. In *Deep carbon* (pp. 4–39). Cambridge University Press.
- DeMeo, F. E., Binzel, R. P., Slivan, S. M., & Bus, S. J. (2009). An extension of the Bus asteroid taxonomy into the near-infrared. *Icarus*, *202*(1), 160–180.
- De Sanctis, M. C., Ammannito, E., Raponi, A., Marchi, S., McCord, T. B., McSween, H. Y., . . . others (2015). Ammoniated phyllosilicates with a likely outer solar system origin on (1) Ceres. *Nature*, *528*(7581), 241–244.
- De Sanctis, M. C., Raponi, A., Ammannito, E., Ciarniello, M., Toplis, M. J., McSween, H. Y., . . . others (2016). Bright carbonate deposits as evidence of aqueous alteration on (1) Ceres. *Nature*, *536*(7614), 54–57.
- Desch, S. J., Kalyaan, A., & Alexander, C. M. O. (2018). The effect of Jupiter’s formation on the distribution of refractory elements and inclusions in meteorites. *The Astrophysical Journal Supplement Series*, *238*(1), 11.
- Dullemond, C. P., Birnstiel, T., Huang, J., Kurtovic, N. T., Andrews, S. M., Guzmán, V. V., . . . others (2018). The disk substructures at high angular resolution project (DSHARP). VI. Dust trapping in thin-ringed protoplanetary disks. *The Astrophysical Journal Letters*, *869*(2), L46.
- Ehlmann, B. L., Hodyss, R., Bristow, T. F., Rossman, G. R., Ammannito, E., De Sanctis, M. C., & Raymond, C. A. (2018). Ambient and cold-temperature infrared spectra and XRD patterns of ammoniated phyllosilicates and carbonaceous chondrite meteorites relevant to Ceres and other solar system bodies. *Meteoritics & Planetary Science*.
- Ermakov, A. I., Fu, R. R., Castillo-Rogez, J. C., Raymond, C. A., Park, R. S., Preusker, F., . . . Zuber, M. T. (2017). Constraints on Ceres’ internal structure and evolution from its shape and gravity measured by the Dawn spacecraft. *Journal of Geophysical Research: Planets*, *122*(11), 2267–2293.
- Fujiya, W., Hoppe, P., Ushikubo, T., Fukuda, K., Lindgren, P., Lee, M. R., . . . Sano, Y. (2019). Migration of D-type asteroids from the outer Solar System inferred from carbonate in meteorites. *Nature Astronomy*, *3*(10), 910–915.
- Fujiya, W., Sugiura, N., Sano, Y., & Hiyagon, H. (2013). Mn–Cr ages of dolomites in CI chondrites and the Tagish lake ungrouped carbonaceous chondrite. *Earth and Planetary Science Letters*, *362*, 130–142.
- Garenne, A., Beck, P., Montes-Hernandez, G., Brissaud, O., Schmitt, B., Quirico, E., . . . Howard, K. (2016). Bidirectional reflectance spectroscopy of carbonaceous chondrites: Implications for water quantification and primary composition. *Icarus*, *264*, 172–183.
- Gassot, O., Panicucci, P., Acciarini, G., Bates, H., Caballero, M., Cambianica, P., . . . others (2021). Calathus: A sample-return mission to Ceres. *Acta Astronautica*, *181*, 112–129.
- Glotch, T. D., & Rossman, G. R. (2009). Mid-infrared reflectance spectra and optical constants of six iron oxide/oxyhydroxide phases. *Icarus*, *204*(2), 663–671.
- Grimm, R. E., & McSween Jr, H. Y. (1989). Water and the thermal evolution of carbonaceous chondrite parent bodies. *Icarus*, *82*(2), 244–280.
- Hapke, B. (2012). *Theory of reflectance and emittance spectroscopy*. Cambridge university press.
- Hasegawa, S., Kuroda, D., Yanagisawa, K., & Usui, F. (2017). Follow-up observations for the asteroid catalog using AKARI spectroscopic observations. *Publications of the Astronomical Society of Japan*, *69*(6), 99.
- Helgeson, H. C., Delany, J. M., Nesbitt, H. W., & Bird, D. K. (1978). Summary and critique of the thermodynamic properties of rock-forming minerals.

- Henderson, P., Henderson, G., et al. (2009). *The Cambridge handbook of Earth science data*. Cambridge University Press Cambridge.
- Hiroi, T., Zolensky, M. E., & Pieters, C. M. (2001). The Tagish Lake meteorite: A possible sample from a D-type asteroid. *Science*, *293*(5538), 2234–2236.
- Hirschmann, M. M., & Dasgupta, R. (2009). The H/C ratios of Earth’s near-surface and deep reservoirs, and consequences for deep Earth volatile cycles. *Chemical Geology*, *262*(1-2), 4–16.
- Hsieh, H. H., & Jewitt, D. (2006). A population of comets in the main asteroid belt. *Science*, *312*(5773), 561–563.
- Hsieh, H. H., Novaković, B., Kim, Y., & Brassier, R. (2018). Asteroid family associations of active asteroids. *The Astronomical Journal*, *155*(2), 96.
- Johansen, A., Blum, J., Tanaka, H., Ormel, C., Bizzarro, M., & Rickman, H. (2014). The multifaceted planetesimal formation process. *Protostars and Planets VI*, 547.
- Johnson, J. W., Oelkers, E. H., & Helgeson, H. C. (1992). SUPCRT92: A software package for calculating the standard molal thermodynamic properties of minerals, gases, aqueous species, and reactions from 1 to 5000 bar and 0 to 1000 °C. *Computers & Geosciences*, *18*(7), 899–947.
- Jones, C. L., & Brearley, A. J. (2006). Experimental aqueous alteration of the Allende meteorite under oxidizing conditions: constraints on asteroidal alteration. *Geochimica et Cosmochimica Acta*, *70*(4), 1040–1058.
- Jutzi, M., Michel, P., Benz, W., & Richardson, D. C. (2010). Fragment properties at the catastrophic disruption threshold: The effect of the parent body’s internal structure. *Icarus*, *207*(1), 54–65.
- Kanagawa, K. D., Muto, T., Tanaka, H., Tanigawa, T., Takeuchi, T., Tsukagoshi, T., & Momose, M. (2015). Mass estimates of a giant planet in a protoplanetary disk from the gap structures. *The Astrophysical Journal Letters*, *806*(1), L15.
- Kaplan, H. H., Lauretta, D. S., Simon, A. A., Hamilton, V. E., DellaGiustina, D. N., Golish, D. R., . . . others (2020). Bright carbonate veins on asteroid (101955) Bennu: Implications for aqueous alteration history. *Science*.
- Kaplan, H. H., Milliken, R. E., & O’D. Alexander, C. M. (2018). New constraints on the abundance and composition of organic matter on Ceres. *Geophysical Research Letters*.
- Kargel, J. S., Croft, S. K., Lunine, J. I., & Lewis, J. S. (1991). Rheological properties of ammonia-water liquids and crystal-liquid slurries: Planetological applications. *Icarus*, *89*(1), 93–112.
- King, T. V. V., Clark, R. N., Calvin, W. M., Sherman, D. M., & Brown, R. H. (1992). Evidence for ammonium-bearing minerals on Ceres. *Science*, *255*(5051), 1551–1553.
- Krot, A. N., Hutcheon, I. D., Brearley, A. J., Pravdivtseva, O. V., Petaev, M. I., & Hohenberg, C. M. (2006). Timescales and settings for alteration of chondritic meteorites. *in Meteorites and the Early Solar System II*, D. S. Lauretta, H. Y. McSween Jr., Eds. (University of Arizona Press, Tucson and Lunar and Planetary Institute), 525–552.
- Krot, A. N., Petaev, M. I., Scott, E. R. D., CHOI, B.-G., Zolensky, M. E., & Keil, K. (1998). Progressive alteration in CV3 chondrites: More evidence for asteroidal alteration. *Meteoritics & Planetary Science*, *33*(5), 1065–1085.
- Krot, A. N., Petaev, M. I., Zolensky, M. E., Keil, K., Scott, E. R. D., & Nakamura, K. (1998). Secondary calcium-iron-rich minerals in the Bali-like and Allende-like oxidized cv3 chondrites and Allende dark inclusions. *Meteoritics & Planetary Science*, *33*(4), 623–645.
- Kruijer, T. S., Burkhardt, C., Budde, G., & Kleine, T. (2017). Age of Jupiter inferred from the distinct genetics and formation times of meteorites. *Proceedings of the National Academy of Sciences*, *114*(26), 6712–6716.

- Kurokawa, H., Ehlmann, B. L., De Sanctis, M. C., Lapôtre, M. G. A., Usui, T., Stein, N. T., . . . Ciarniello, M. (2020). A probabilistic approach to determination of Ceres' average surface composition from Dawn visible-infrared mapping spectrometer and gamma ray and neutron detector data. *Journal of Geophysical Research: Planets*, *125*(12), e2020JE006606.
- Lapotre, M. G. A., Ehlmann, B. L., & Minson, S. E. (2017). A probabilistic approach to remote compositional analysis of planetary surfaces. *Journal of Geophysical Research: Planets*, *122*(5), 983–1009.
- Lauretta, D. S., Balram-Knutson, S. S., Beshore, E., Boynton, W. V., d'Aubigny, C. D., DellaGiustina, D. N., . . . others (2017). OSIRIS-REx: sample return from asteroid (101955) Bennu. *Space Science Reviews*, *212*(1-2), 925–984.
- Lawrence, S. J., & Lucey, P. G. (2007). Radiative transfer mixing models of meteoritic assemblages. *Journal of Geophysical Research: Planets*, *112*(E7).
- Lee, M. R., Lindgren, P., Sofe, M. R., Alexander, C. M. O., & Wang, J. (2012). Extended chronologies of aqueous alteration in the CM2 carbonaceous chondrites: Evidence from carbonates in Queen Alexandra Range 93005. *Geochimica et Cosmochimica Acta*, *92*, 148–169.
- Lee, M. R., Sofe, M. R., Lindgren, P., Starkey, N. A., & Franchi, I. A. (2013). The oxygen isotope evolution of parent body aqueous solutions as recorded by multiple carbonate generations in the Lonewolf Nunataks 94101 CM2 carbonaceous chondrite. *Geochimica et Cosmochimica Acta*, *121*, 452–466.
- Li, J.-Y., Schröder, S. E., Mottola, S., Nathues, A., Castillo-Rogez, J. C., Schorghofer, N., . . . others (2019). Spectrophotometric modeling and mapping of Ceres. *Icarus*, *322*, 144–167.
- Lucey, P. G. (1998). Model near-infrared optical constants of olivine and pyroxene as a function of iron content. *Journal of Geophysical Research: Planets*, *103*(E1), 1703–1713.
- Machida, R., & Abe, Y. (2010). Terrestrial planet formation through accretion of sublimating icy planetesimals in a cold nebula. *The Astrophysical Journal*, *716*(2), 1252.
- Mao, X., & McKinnon, W. B. (2018). Faster paleospin and deep-seated uncompensated mass as possible explanations for Ceres' present-day shape and gravity. *Icarus*, *299*, 430–442.
- Marchi, S., Raponi, A., Prettyman, T. H., De Sanctis, M. C., Castillo-Rogez, J., Raymond, C. A., . . . others (2019). An aqueously altered carbon-rich Ceres. *Nature Astronomy*, *3*(2), 140–145.
- Marion, G. M., & Kargel, J. S. (2007). *Cold aqueous planetary geochemistry with FREZCHEM: from modeling to the search for life at the limits*. Springer Science & Business Media.
- Marion, G. M., Kargel, J. S., Catling, D. C., & Lunine, J. I. (2012). Modeling ammonia–ammonium aqueous chemistries in the Solar System's icy bodies. *Icarus*, *220*(2), 932–946.
- Marrocchi, Y., Bekaert, D. V., & Piani, L. (2018). Origin and abundance of water in carbonaceous asteroids. *Earth and Planetary Science Letters*, *482*, 23–32.
- Mastrapa, R. M., Sandford, S. A., Roush, T. L., Cruikshank, D. P., & Dalle Ore, C. M. (2009). Optical constants of amorphous and crystalline H₂O-ice: 2.5–22 μm (4000–455 cm^{-1}) optical constants of H₂O-ice. *The Astrophysical Journal*, *701*(2), 1347.
- McAlister, J. A., & Kettler, R. M. (2008). Metastable equilibria among dicarboxylic acids and the oxidation state during aqueous alteration on the CM2 chondrite parent body. *Geochimica et Cosmochimica Acta*, *72*(1), 233–241.
- McCollom, T. M., & Bach, W. (2009). Thermodynamic constraints on hydrogen generation during serpentinization of ultramafic rocks. *Geochimica et Cosmochimica Acta*, *73*(3), 856–875.
- McSween Jr, H. Y., Emery, J. P., Rivkin, A. S., Toplis, M. J., C. Castillo-Rogez,

- J., Prettyman, T. H., ... Russell, C. T. (2018). Carbonaceous chondrites as analogs for the composition and alteration of Ceres. *Meteoritics & Planetary Science*, 53(9), 1793–1804.
- McSween Jr, H. Y., Ghosh, A., Grimm, R. E., Wilson, L., & Young, E. D. (2002). Thermal evolution models of asteroids. *Asteroids III*, 559.
- Milliken, R. E., & Rivkin, A. S. (2009). Brucite and carbonate assemblages from altered olivine-rich materials on Ceres. *Nature Geoscience*, 2(4), 258–261.
- Mironenko, M. V., Grant, S. A., Marion, G. M., & Farren, R. E. (1997). *FREZCHEM2 A chemical thermodynamic model for electrolyte solutions at subzero temperatures* (Tech. Rep.). Cold Regions Research and Engineering Lab, Hanover, NH.
- Morbidelli, A. (2020). Planet formation by pebble accretion in ringed disks. *Astronomy & Astrophysics*, 638, A1.
- Mumma, M. J., & Charnley, S. B. (2011). The chemical composition of comets—emerging taxonomies and natal heritage. *Annual Review of Astronomy and Astrophysics*, 49, 471–524.
- Nara, Y., Okuzumi, S., & Kurokawa, H. (2019). Delivery of ammonia ice to Ceres by pebble accretion. *AAS/Division for Extreme Solar Systems Abstracts*, 51, 317–19.
- Neveu, M., & Desch, S. J. (2015). Geochemistry, thermal evolution, and cryovolcanism on Ceres with a muddy ice mantle. *Geophysical Research Letters*, 42(23), 10–197.
- Neveu, M., Desch, S. J., & Castillo-Rogez, J. C. (2017). Aqueous geochemistry in icy world interiors: Equilibrium fluid, rock, and gas compositions, and fate of antifreezes and radionuclides. *Geochimica et Cosmochimica Acta*, 212, 324–371.
- Nittler, L. R., Stroud, R. M., Trigo-Rodríguez, J. M., De Gregorio, B. T., Alexander, C. M., Davidson, J., ... Tanbakouei, S. (2019). A cometary building block in a primitive asteroidal meteorite. *Nature Astronomy*, 3(7), 659–666.
- Okuzumi, S., Momose, M., Sirono, S.-i., Kobayashi, H., & Tanaka, H. (2016). Sintering-induced dust ring formation in protoplanetary disks: Application to the HL tau disk. *The Astrophysical Journal*, 821(2), 82.
- Okuzumi, S., Tanaka, H., Kobayashi, H., & Wada, K. (2012). Rapid coagulation of porous dust aggregates outside the snow line: A pathway to successful icy planetesimal formation. *The Astrophysical Journal*, 752(2), 106.
- Ozdemir, O., Celik, M. S., Nickolov, Z. S., & Miller, J. D. (2007). Water structure and its influence on the flotation of carbonate and bicarbonate salts. *Journal of Colloid and Interface Science*, 314(2), 545–551.
- Palandri, J. L., & Kharaka, Y. K. (2004). *A compilation of rate parameters of water-mineral interaction kinetics for application to geochemical modeling* (Tech. Rep.). Geological Survey Menlo Park CA.
- Palguta, J., Schubert, G., & Travis, B. J. (2010). Fluid flow and chemical alteration in carbonaceous chondrite parent bodies. *Earth and Planetary Science Letters*, 296(3–4), 235–243.
- Park, R. S., Konopliv, A. S., Bills, B. G., Rambaux, N., Castillo-Rogez, J. C., Raymond, C. A., ... others (2016). A partially differentiated interior for (1) Ceres deduced from its gravity field and shape. *Nature*, 537(7621), 515–517.
- Pearson, V. K., Sephton, M. A., Franchi, I. A., Gibson, J. M., & Gilmour, I. (2006). Carbon and nitrogen in carbonaceous chondrites: Elemental abundances and stable isotopic compositions. *Meteoritics & Planetary Science*, 41(12), 1899–1918.
- Pizzarello, S., & Williams, L. (2012). Ammonia in the early solar system: An account from carbonaceous meteorites. *The Astrophysical Journal*, 749(2), 161.
- Pollack, J. B., Hollenbach, D., Beckwith, S., Simonelli, D. P., Roush, T., & Fong, W. (1994). Composition and radiative properties of grains in molecular clouds and

- accretion disks. *The Astrophysical Journal*, *421*, 615–639.
- Prettyman, T. H., Yamashita, N., Toplis, M. J., McSween, H. Y., Schörghofer, N., Marchi, S., . . . others (2017). Extensive water ice within Ceres' aqueously altered regolith: Evidence from nuclear spectroscopy. *Science*, *355*(6320), 55–59.
- Raponi, A., De Sanctis, M. C., Carrozzo, F. G., Ciarniello, M., Castillo-Rogez, J., Ammannito, E., . . . others (2019). Mineralogy of Occator crater on Ceres and insight into its evolution from the properties of carbonates, phyllosilicates, and chlorides. *Icarus*, *320*, 83–96.
- Rivkin, A. S., Asphaug, E., & Bottke, W. F. (2014). The case of the missing Ceres family. *Icarus*, *243*, 429–439.
- Rivkin, A. S., Campins, H., Emery, J. P., Howell, E. S., Licandro, J., Takir, D., & Vilas, F. (2015). Astronomical observations of volatiles on asteroids. *Asteroids IV*, 65–87.
- Rivkin, A. S., Davies, J. K., Johnson, J. R., Ellison, S. L., Trilling, D. E., Brown, R. H., & Lebofsky, L. A. (2003). Hydrogen concentrations on C-class asteroids derived from remote sensing. *Meteoritics & Planetary Science*, *38*(9), 1383–1398.
- Rivkin, A. S., & Emery, J. P. (2010). Detection of ice and organics on an asteroidal surface. *Nature*, *464*(7293), 1322–1323.
- Rivkin, A. S., Howell, E. S., & Emery, J. P. (2019). Infrared spectroscopy of large, low-albedo asteroids: Are Ceres and Themis archetypes or outliers? *Journal of Geophysical Research: Planets*, *124*(5), 1393–1409.
- Rivkin, A. S., Thomas, C. A., Howell, E. S., & Emery, J. P. (2015). The Ch-class asteroids: Connecting a visible taxonomic class to a 3 μm band shape. *The Astronomical Journal*, *150*(6), 198.
- Rivkin, A. S., Volquardsen, E. L., & Clark, B. E. (2006). The surface composition of Ceres: Discovery of carbonates and iron-rich clays. *Icarus*, *185*(2), 563–567.
- Roatsch, T., Kersten, E., Matz, K.-D., Preusker, F., Scholten, F., Jaumann, R., . . . Russell, C. T. (2016). High-resolution Ceres high altitude mapping orbit atlas derived from dawn framing camera images. *Planetary and Space Science*, *129*, 103–107.
- Rosenberg, N. D., Browning, L., & Bourcier, W. L. (2001). Modeling aqueous alteration of CM carbonaceous chondrites. *Meteoritics & Planetary Science*, *36*(2), 239–244.
- Rubin, A. E. (1997a). Mineralogy of meteorite groups. *Meteoritics & Planetary Science*, *32*(2), 231–247.
- Rubin, A. E. (1997b). Mineralogy of meteorite groups: An update. *Meteoritics & Planetary Science*, *32*(5), 733–734.
- Rubin, A. E. (2012). Collisional facilitation of aqueous alteration of CM and CV carbonaceous chondrites. *Geochimica et Cosmochimica Acta*, *90*, 181–194.
- Rubin, A. E., Trigo-Rodríguez, J. M., Huber, H., & Wasson, J. T. (2007). Progressive aqueous alteration of CM carbonaceous chondrites. *Geochimica et Cosmochimica Acta*, *71*(9), 2361–2382.
- Rubin, A. E., Zolensky, M. E., & Bodnar, R. J. (2002). The halite-bearing Zag and Monahans (1998) meteorite breccias: Shock metamorphism, thermal metamorphism and aqueous alteration on the H-chondrite parent body. *Meteoritics & Planetary Science*, *37*(1), 125–141.
- Rubin, M., Enggrand, C., Snodgrass, C., Weissman, P., Altwegg, K., Busemann, H., . . . Mumma, M. (2020). On the origin and evolution of the material in 67P/Churyumov-Gerasimenko. *Space science reviews*, *216*(5), 1–43.
- Sato, K. (1984). Reflectivity spectra and optical constants of pyrites (FeS_2 , CoS_2 and NiS_2) between 0.2 and 4.4 eV. *Journal of the Physical Society of Japan*, *53*(5), 1617–1620.

- Sato, T., Okuzumi, S., & Ida, S. (2016). On the water delivery to terrestrial embryos by ice pebble accretion. *Astronomy & Astrophysics*, *589*, A15.
- Schorghofer, N. (2008). The lifetime of ice on main belt asteroids. *The Astrophysical Journal*, *682*(1), 697.
- Schulte, M., & Shock, E. (2004). Coupled organic synthesis and mineral alteration on meteorite parent bodies. *Meteoritics & Planetary Science*, *39*(9), 1577–1590.
- Shock, E. L., & Helgeson, H. C. (1988). Calculation of the thermodynamic and transport properties of aqueous species at high pressures and temperatures: Correlation algorithms for ionic species and equation of state predictions to 5 kb and 1000 °C. *Geochimica et Cosmochimica Acta*, *52*(8), 2009–2036.
- Shock, E. L., Helgeson, H. C., & Sverjensky, D. A. (1989). Calculation of the thermodynamic and transport properties of aqueous species at high pressures and temperatures: Standard partial molal properties of inorganic neutral species. *Geochimica et Cosmochimica Acta*, *53*(9), 2157–2183.
- Shock, E. L., & Koretsky, C. M. (1995). Metal-organic complexes in geochemical processes: Estimation of standard partial molal thermodynamic properties of aqueous complexes between metal cations and monovalent organic acid ligands at high pressures and temperatures. *Geochimica et Cosmochimica Acta*, *59*(8), 1497–1532.
- Shock, E. L., Sassani, D. C., Willis, M., & Sverjensky, D. A. (1997). Inorganic species in geologic fluids: correlations among standard molal thermodynamic properties of aqueous ions and hydroxide complexes. *Geochimica et Cosmochimica Acta*, *61*(5), 907–950.
- Stein, N. T., Ehlmann, B. L., Palomba, E., De Sanctis, M. C., Nathues, A., Hiesinger, H., ... others (2019). The formation and evolution of bright spots on Ceres. *Icarus*, *320*, 188–201.
- Sverjensky, D. A., Shock, E. L., & Helgeson, H. C. (1997). Prediction of the thermodynamic properties of aqueous metal complexes to 1000 °C and 5 kb. *Geochimica et Cosmochimica Acta*, *61*(7), 1359–1412.
- Taki, T., Kuwabara, K., Kobayashi, H., & Suzuki, T. K. (2021). New growth mechanism of dust grains in protoplanetary disks with magnetically driven disk winds. *The Astrophysical Journal*, *909*(1), 75.
- Takir, D., & Emery, J. P. (2012). Outer main belt asteroids: Identification and distribution of four 3- μ m spectral groups. *Icarus*, *219*(2), 641–654.
- Tanbakouei, S., Trigo-Rodríguez, J. M., Blum, J., Williams, I., & Llorca, J. (2020). Comparing the reflectivity of ungrouped carbonaceous chondrites with those of short-period comets like 2P/Encke. *Astronomy & Astrophysics*, *641*, A58.
- Tominaga, R. T., Takahashi, S. Z., & Inutsuka, S.-i. (2019). Revised description of dust diffusion and a new instability creating multiple rings in protoplanetary disks. *The Astrophysical Journal*, *881*(1), 53.
- Tosaka, H., Itoh, K., & Furuno, T. (2000). Fully coupled formulation of surface flow with 2-phase subsurface flow for hydrological simulation. *Hydrological processes*, *14*(3), 449–464.
- Trang, D., Thompson, M. S., Clark, B. E., Kaplan, H. H., Zou, X.-D., Li, J.-Y., ... others (2021). The role of hydrated minerals and space weathering products in the bluing of carbonaceous asteroids. *The Planetary Science Journal*, *2*(2), 68.
- Travis, B. J., Bland, P. A., Feldman, W. C., & Sykes, M. V. (2018). Hydrothermal dynamics in a CM-based model of Ceres. *Meteoritics & Planetary Science*, *53*(9), 2008–2032.
- Travis, B. J., & Schubert, G. (2005). Hydrothermal convection in carbonaceous chondrite parent bodies. *Earth and Planetary Science Letters*, *240*(2), 234–250.
- Trigo-Rodríguez, J. M. (2015). Aqueous alteration in chondritic asteroids and

- comets from the study of carbonaceous chondrites. *Planetary Materials. EMU Notes in Mineralogy*, 15, 67–87.
- Trigo-Rodríguez, J. M., Moyano-Camero, C. E., Llorca, J., Fornasier, S., Barucci, M. A., Belskaya, I., ... others (2014). UV to far-IR reflectance spectra of carbonaceous chondrites—I. Implications for remote characterization of dark primitive asteroids targeted by sample-return missions. *Monthly Notices of the Royal Astronomical Society*, 437(1), 227–240.
- Trigo-Rodríguez, J. M., Rimola, A., Tanbakouei, S., Soto, V. C., & Lee, M. (2019). Accretion of water in carbonaceous chondrites: Current evidence and implications for the delivery of water to early Earth. *Space Science Reviews*, 215(1), 1–27.
- Trigo-Rodríguez, J. M., & Rubin, A. E. (2006). Evidence for parent-body aqueous flow in the MET 01070 CM carbonaceous chondrite. In *37th Annual Lunar and Planetary Science Conference* (p. 1104).
- Trigo-Rodríguez, J. M., Rubin, A. E., & Wasson, J. T. (2006). Non-nebular origin of dark mantles around chondrules and inclusions in CM chondrites. *Geochimica et Cosmochimica Acta*, 70(5), 1271–1290.
- Tsuchiyama, A., Miyake, A., Okuzumi, S., Kitayama, A., Kawano, J., Uesugi, K., ... Zolensky, M. (2021). Discovery of primitive CO₂-bearing fluid in an aqueously altered carbonaceous chondrite. *Science Advances*, 7(17), eabg9707.
- Usui, F., Hasegawa, S., Ootsubo, T., & Onaka, T. (2019). AKARI/IRC near-infrared asteroid spectroscopic survey: AcuA-spec. *Publications of the Astronomical Society of Japan*, 71(1), 1.
- Vernazza, P., Castillo-Rogez, J., Beck, P., Emery, J., Brunetto, R., Delbo, M., ... others (2017). Different origins or different evolutions? Decoding the spectral diversity among C-type asteroids. *The Astronomical Journal*, 153(2), 72.
- Vernazza, P., Ferrais, M., Jorda, L., Hanuš, J., Carry, B., Marsset, M., ... others (2021). VLT/SPHERE imaging survey of the largest main-belt asteroids: Final results and synthesis. *Astronomy & Astrophysics*, 654, A56.
- Vernazza, P., Fulvio, D., Brunetto, R., Emery, J. P., Dukes, C., Cipriani, F., ... others (2013). Paucity of Tagish Lake-like parent bodies in the Asteroid Belt and among Jupiter Trojans. *Icarus*, 225(1), 517–525.
- Vernazza, P., Jorda, L., Ševeček, P., Brož, M., Viikinkoski, M., Hanuš, J., ... others (2020). A basin-free spherical shape as an outcome of a giant impact on asteroid Hygiea. *Nature Astronomy*, 4(2), 136–141.
- Wakita, S., & Genda, H. (2019). Fates of hydrous materials during planetesimal collisions. *Icarus*, 328, 58–68.
- Wakita, S., & Sekiya, M. (2011). Thermal evolution of icy planetesimals in the solar nebula. *Earth, planets and space*, 63(12), 1193–1206.
- Walsh, K. J., Morbidelli, A., Raymond, S. N., O’Brien, D. P., & Mandell, A. M. (2011). A low mass for mars from jupiter’s early gas-driven migration. *Nature*, 475(7355), 206–209.
- Watanabe, S., Hirabayashi, M., Hirata, N., Hirata, N., Noguchi, R., Shimaki, Y., ... others (2019). Hayabusa2 arrives at the carbonaceous asteroid 162173 Ryugu—A spinning top-shaped rubble pile. *Science*, 364(6437), 268–272.
- Whitby, J., Burgess, R., Turner, G., Gilmour, J., & Bridges, J. (2000). Extinct 129I in halite from a primitive meteorite: Evidence for evaporite formation in the early solar system. *Science*, 288(5472), 1819–1821.
- Wilson, J., Savage, D., Cuadros, J., Shibata, M., & Ragnarsdottir, K. V. (2006). The effect of iron on montmorillonite stability.(i) Background and thermodynamic considerations. *Geochimica et Cosmochimica Acta*, 70(2), 306–322.
- Wolery, T. W., & Jarek, R. L. (2003). Software user’s manual. *EQ3/6, version, 8*, 376.
- Young, E. D. (2001). The hydrology of carbonaceous chondrite parent bodies and the evolution of planet progenitors. *Philosophical Transactions of the Royal*

- Society of London. Series A: Mathematical, Physical and Engineering Sciences*, 359(1787), 2095–2110.
- Young, E. D., Ash, R. D., England, P., & Rumble, D. (1999). Fluid flow in chondritic parent bodies: Deciphering the compositions of planetesimals. *Science*, 286(5443), 1331–1335.
- Young, E. D., Zhang, K. K., & Schubert, G. (2003). Conditions for pore water convection within carbonaceous chondrite parent bodies—implications for planetesimal size and heat production. *Earth and Planetary Science Letters*, 213(3-4), 249–259.
- Zolensky, M., Barrett, R., & Browning, L. (1993). Mineralogy and composition of matrix and chondrule rims in carbonaceous chondrites. *Geochimica et Cosmochimica Acta*, 57(13), 3123–3148.
- Zolensky, M. E., Bodnar, R. J., Gibson, E. K., Nyquist, L. E., Reese, Y., Shih, C.-Y., & Wiesmann, H. (1999). Asteroidal water within fluid inclusion-bearing halite in an H5 chondrite, Monahans (1998). *Science*, 285(5432), 1377–1379.
- Zolensky, M. E., Bourcier, W. L., & Gooding, J. L. (1989). Aqueous alteration on the hydrous asteroids: Results of EQ3/6 computer simulations. *Icarus*, 78(2), 411–425.
- Zolotov, M. Y. (2012). Aqueous fluid composition in CI chondritic materials: Chemical equilibrium assessments in closed systems. *Icarus*, 220(2), 713–729.
- Zolotov, M. Y. (2017). Aqueous origins of bright salt deposits on Ceres. *Icarus*, 296, 289–304.
- Zolotov, M. Y. (2020). The composition and structure of Ceres’ interior. *Icarus*, 335, 113404.